PHYSICAL REVIEW D **78,** 084033 (2008)

Accurate evolutions of inspiralling neutron-star binaries: Prompt and delayed collapse to a black hole

Luca Baiotti,[1,2] Bruno Giacomazzo,[2] and Luciano Rezzolla[2,3,4]

[1]*Graduate School of Arts and Sciences, University of Tokyo, Komaba, Meguro-ku, Tokyo, 153-8902, Japan*
[2]*Max-Planck-Institut für Gravitationsphysik, Albert-Einstein-Institut, Potsdam-Golm, Germany*
[3]*Department of Physics and Astronomy, Louisiana State University, Baton Rouge, Louisiana, USA*
[4]*INFN, Department of Physics, University of Trieste, Trieste, Italy*

(Received 3 April 2008; published 24 October 2008)

Binary neutron-star systems represent primary sources for the gravitational-wave detectors that are presently operating or are close to being operating at the target sensitivities. We present a systematic investigation in full general relativity of the dynamics and gravitational-wave emission from binary neutron stars which inspiral and merge, producing a black hole surrounded by a torus. Our results represent the state of the art from several points of view: (i) We use high-resolution shock-capturing methods for the solution of the hydrodynamics equations and high-order finite-differencing techniques for the solution of the Einstein equations; (ii) We employ adaptive mesh-refinement techniques with ''moving boxes'' that provide high-resolution around the orbiting stars; (iii) We use as initial data accurate solutions of the Einstein equations for a system of binary neutron stars in irrotational quasicircular orbits; (iv) We exploit the isolated-horizon formalism to measure the properties of the black holes produced in the merger; (v) Finally, we use two approaches, based either on gauge-invariant perturbations or on Weyl scalars, to calculate the gravitational waves emitted by the system. Within our idealized treatment of the matter, these techniques allow us to perform accurate evolutions on time scales never reported before (i.e. $\sim$30 ms) and to provide the first complete description of the inspiral and merger of a neutron-star binary leading to the *prompt* or *delayed* formation of a black hole and to its ringdown. We consider either a polytropic equation of state or that of an ideal fluid and show that already with this idealized treatment a very interesting phenomenology can be described. In particular, we show that while higher-mass polytropic binaries lead to the *prompt* formation of a rapidly rotating black hole surrounded by a dense torus, lower-mass binaries give rise to a differentially rotating star, which undergoes large oscillations and emits large amounts of gravitational radiation. Eventually, also the hyper-massive neutron star collapses to a rotating black hole surrounded by a torus. Finally, we also show that the use of a nonisentropic equation of state leads to significantly different evolutions, giving rise to a *delayed* collapse also with high-mass binaries, as well as to a more intense emission of gravitational waves and to a geometrically thicker torus.

DOI: 10.1103/PhysRevD.78.084033 PACS numbers: 04.30.Db, 04.40.Dg, 95.30.Lz, 97.60.Jd

I. INTRODUCTION

Little is required to justify the efforts in the study of binary systems. Despite the simplicity of its formulation, the relativistic two-body problem is, in fact, one of the most challenging problems in classical general relativity. Furthermore, binary systems of compact objects are considered one of the most important sources for gravitational-wave emission and are thought to be at the origin of some of the most violent events in the Universe. While some of the numerical difficulties involved in the simulations of such highly dynamical systems have been overcome in the case of binary black holes (BHs), numerical simulations of binary neutron stars (NSs) in general relativity have so far provided only rudimentary descriptions of the complex physics accompanying the inspiral and merger. Simulations of this type are the focus of this paper.

Binary NSs are known to exist and for some of the systems in our own galaxy general-relativistic effects in the binary orbit have been measured to high precision [1–3]. The inspiral and merger of two NSs in binary orbit is the inevitable fate of close-binary evolution, whose main dissipation mechanism is the emission of gravitational radiation. An important part of the interest in the study of coalescing systems of compact objects comes from the richness of general-relativistic effects that accompany these processes and, most importantly, from the gravitational-wave emission. Detection of gravitational waves from NS binaries will indeed provide a wide variety of physical information on the component stars, including their mass, spin, radius, and equations of state (EOS) [4,5]. Furthermore, NS binary systems are expected to produce signals of amplitude large enough to be relevant for Earth-based gravitational-wave detectors and to be sufficiently frequent sources to be detectable over the time scale in which the detectors are operative. Recent improved extrapolations to the local group of the estimated galactic coalescence rates predict 1 event per 3–10 years for the first generation of interferometric detectors and of 10–50 events per year, for the generation of advanced detectors [6].

There are three possible characteristic gravitational-wave frequencies related to the inspiral and merger of binary systems. The first one is the frequency of the orbital motion of the stars in the last stages of the inspiral, before tidal distortions become important. The second characteristic frequency is associated with the fundamental oscillation modes of the merged massive object formed after the onset of the merger. Numerical simulations in the frameworks of Newtonian [7], post-Newtonian (PN) [8], semi-relativistic [9], and fully general-relativistic gravity [10] have shown that, if a BH is not produced promptly, the frequency of the fundamental oscillation modes of the merged object is between 2 and 3 kHz, depending on the EOS and on the initial compactness of the progenitor NSs. Finally, the third frequency is that of the quasinormal modes (QNMs) of the BH, which is eventually formed after the merger.

The study of NS binary systems goes beyond the impact it has on gravitational-wave astronomy and is also finalized to the understanding of the origin of some type of γ-ray bursts (GRBs), whose short rise times suggest that their central sources have to be highly relativistic objects [11]. After the observational confirmation that GRBs have a cosmological origin, it has been estimated that the central sources powering these bursts must provide a large amount of energy ($\sim 10^{51}$ ergs) in a very short time scale, going from 1 ms to 1 s (at least for a subclass of them, called ''short'' GRBs). It has been suggested that the merger of NS binaries could be a likely candidate for the powerful central source of a subclass of short GRBs. The typical scenario is based on the assumption that a system composed of a rotating BH and a surrounding massive torus is formed after the merger. If the disc had a mass $\gtrsim 0.1 M_{\odot}$, it could supply the large amount of energy by neutrino processes or by extracting the rotational energy of the BH.

The understanding of GRBs is therefore an additional motivation to investigate the final fate of binaries after the merger. The total gravitational masses of the known galactic NS binary systems are in a narrow range $\sim$2.65–2.85$M_{\odot}$ and the present observational evidence indicates that the masses of the two stars are nearly equal. If this is the general situation, NSs in binary systems will not be tidally disrupted before the merger. As a result, the mass loss from the binary systems is expected to be small during the evolution and the mass of the merged object will be approximately equal to the initial mass of the binary system. Since the maximum allowed gravitational mass for spherical NSs is in the range $\sim$1.5–2.3$M_{\odot}$, depending on the EOS, the compact objects formed just after the merger of these binary systems are expected to collapse to a BH, either promptly after the merger or after a certain ''delay.'' Indeed, if the merged object rotates differentially, the final collapse may be prevented on a time scale over which dissipative effects like viscosity, magnetic fields, or gravitational-wave emission bring the star towards a configuration which is unstable to gravitational collapse. During this process, if the merged object has a sufficiently high ratio of rotational energy to the gravitational binding energy, it could also become dynamically unstable to nonlinear instabilities, such as the bar-mode instability [12,13]. It is quite clear, therefore, that while the asymptotic end state of a binary NS system is a rotating BH, the properties of the intermediate product of the merger are still pretty much an open question, depending not only on the nuclear EOS for high-density neutron matter, but also on the rotational profile of the merged object and on the physical processes through which the object can lose angular momentum and energy.

Several different approaches have been developed over the years to tackle the binary NS problem. One of these approaches attempts to estimate the properties of the binary evolution by considering sequences of quasiequilibrium configurations, that is by neglecting both gravitational waves and wave-induced deviations from a circular orbit; this is expected to be a very good approximation if the stars are well separated [14–26]. Other approaches have tried to simplify some aspects of the coalescence, by solving, for instance, the Newtonian or PN version of the hydrodynamics equations (see [7,8,27–33] and references therein). At the same time, alternative treatments of the gravitational fields, such as the conformally flat approximation, have been developed and coupled to the solution of the relativistic hydrodynamical equations [34,35], either in the fluid approximation or in its smooth-particle hydrodynamics (SPH) variant [36]. Special attention has also been paid to the role played in these calculations by the EOS and progress has been made recently with SPH calculations [4,5].

While all of the above-mentioned works have provided insight into the coalescence process and some of them represent the state of the art for their realistic treatment of the matter properties [4,5], they are nevertheless only approximations to the full general-relativistic solution. The latter is, however, required for quantitatively reliable coalescence waveforms and to determine those qualitative features of the final merger which can only result from strong-field effects.

Several groups have launched efforts to solve the equations of relativistic hydrodynamics together with the Einstein equations and to model the coalescence and merger of NS binaries [37–40]. The first successful simulations of binary NS mergers were those of Shibata and Uryu [41–43]. Later on, Shibata and Taniguchi have extended their numerical studies to unequal-mass binaries providing a detailed and accurate discussion of simulations performed with realistic EOSs (see [44] and references therein). More recently, Anderson *et al.* [45] have made important technical progress by presenting results of binary NS evolutions using an adaptive-mesh-refinement (AMR) code. However, despite the high resolution avail-

able with the use of AMR, no waveforms from the BH formation were reported in Ref. [45] over the time scales discussed for the evolutions. Finally, a set of simulations involving (among other compact binaries) also binary neutron stars have been recently presented by Yamamoto *et al.* using AMR techniques with moving boxes [46].

An aspect common to all the above-mentioned simulations is that, while they represent enormous progress with respect to what was possible to calculate only a few years ago, they provide a description of the dynamics which is limited to a few ms after the merger. The work presented here aims at pushing this limit further and to provide a systematic investigation of the inspiral, but also of the merger and of the (possibly) delayed collapse to a BH. Despite the fact that we do not account for the transport of radiation or neutrinos, our results benefit from a number of technical advantages (some of which are also shared by other groups): (i) The use of high-resolution shock-capturing methods for the solution of the hydrodynamics equations and high-order (i.e. fourth order in space and third order in time) finite-differencing techniques for the solution of the Einstein equations; (ii) The use of adaptive mesh-refinement techniques that provide higher resolution around the orbiting stars; (iii) The use of consistent initial data representing a system of binary NSs in irrotational quasicircular orbits; (iv) The use of the isolated-horizon formalism to measure the properties of the BHs produced in the merger; (v) The use of two complementary approaches for the extraction of the gravitational waves produced. Most importantly, however, our simulations can rely on unprecedented evolution time scales spanning more than 30 ms.

Exploiting these features we provide, within an idealized treatment of the matter, the first complete description of the inspiral and merger of a NS binary leading to the *prompt* or *delayed* formation of a BH and to its ringdown. While our treatment of the matter is simplified with the use of analytic EOSs, we show that this does not prevent us from reproducing some of the most salient aspects that more realistic EOSs would yield. In particular, we show that an isentropic (i.e. polytropic) EOS leads either to the *prompt* formation of a rapidly rotating BH surrounded by a dense torus if the binary is sufficiently massive, or, if the binary is not very massive, to a differentially rotating star, which undergoes oscillations, emitting large amounts of gravitational radiation and experiencing a *delayed* collapse to BH. In addition, we show that the use of nonisentropic (i.e. ideal-fluid) EOS inevitably leads to a further delay in the collapse to BH, as a result of the larger pressure support provided by the temperature increase via shocks.

Our interest also goes to the small-scale hydrodynamics of the merger and to the possibility that dynamical instabilities develop. In particular, we show that, irrespective of the EOS used, coalescing irrotational NSs form a vortex sheet when the outer layers of the stars come into contact. This interface is Kelvin-Helmholtz unstable on all wavelengths (see, e.g., [47] and references therein) and, exploiting the use of AMR techniques, we provide a first quantitative description of this instability in general-relativistic simulations.

Special attention in this work is obviously dedicated to the analysis of the waveforms produced and to their properties for the different configurations. In particular, we find that the largest loss rates of energy and angular momentum via gravitational radiation develop at the time of the collapse to BH and during the first stages of the subsequent ringdown. Nevertheless, the configurations which emit the highest amount of energy and angular momentum are those with lower mass, because they do not collapse promptly to a BH, but instead produce a violently oscillating transient object, which produces copious gravitational radiation while rearranging its angular-momentum distribution. We also show that, although the gravitational-wave emission from NS binaries has spectral distributions with large powers at high frequencies (i.e. $f \gtrsim 1$ kHz), a signal-to-noise ratio (SNR) as large as 3 can be estimated for a source at 10 Mpc if using the sensitivity of currently operating gravitational-wave interferometric detectors.

Many aspects of the simulations reported here could be improved and probably the most urgent among them is the inclusion of magnetic fields. Recent calculations have shown that the corrections produced by strong magnetic fields could be large and are very likely to be present [see Ref. [48] for Newtonian magnetohydrodynamical (MHD) simulations and Refs. [49,50] for a recent general-relativistic extension]. While we have already developed the numerical code that would allow to perform the study of such binaries in the ideal-MHD limit [51], our analysis is here limited to unmagnetized NSs.

The paper is organized as follows. In Sec. II we first summarize the formalism we adopt for the numerical solution of the Einstein and of the relativistic-hydrodynamics equations; we then describe briefly the numerical methods we implemented in the `Whisky` code [52,53], we outline our mesh-refined grid setup, and we finally describe the quasiequilibrium initial data we use. In Secs. III A and III B we describe binaries evolved with the polytropic EOS and having a comparatively "high" or "low" mass, respectively. In Secs. III C and III D we instead discuss the dynamics of the same initial models when evolved with the ideal-fluid EOS, while Sec. III E is dedicated to our analysis of the Kelvin-Helmholtz instability. In Secs. IV A and IV B we characterize the gravitational-wave emission for the case of the polytropic and ideal-fluid EOS, respectively. Finally in Secs. IV C and IV D we report about the energy and angular momentum carried by the gravitational waves and their power spectra. In the appendix, further comments on numerical and technical issues are discussed.

We here use a spacelike signature $(-, +, +, +)$ and a system of units in which $c = G = M_\odot = 1$ (unless explic-

itly shown otherwise for convenience). Greek indices are taken to run from 0 to 3, Latin indices from 1 to 3, and we adopt the standard convention for the summation over repeated indices.

II. MATHEMATICAL AND NUMERICAL SETUP

A. Evolution system for the fields

We evolve a conformal-traceless "3 + 1" formulation of the Einstein equations [54–57], in which the spacetime is decomposed into three-dimensional spacelike slices, described by a metric γ_{ij}, its embedding in the full spacetime, specified by the extrinsic curvature K_{ij}, and the gauge functions α (lapse) and β^i (shift) that specify a coordinate frame (see Sec. II B for details on how we treat gauges and [58] for a general description of the 3 + 1 split). The particular system which we evolve transforms the standard ADM variables as follows. The three-metric γ_{ij} is conformally transformed via

$$\phi = \tfrac{1}{12}\ln\det\gamma_{ij}, \qquad \tilde{\gamma}_{ij} = e^{-4\phi}\gamma_{ij}, \tag{1}$$

and the conformal factor ϕ is evolved as an independent variable, whereas $\tilde{\gamma}_{ij}$ is subject to the constraint $\det\tilde{\gamma}_{ij} = 1$. The extrinsic curvature is subjected to the same conformal transformation and its trace $\mathrm{tr}K_{ij}$ is evolved as an independent variable. That is, in place of K_{ij} we evolve:

$$K \equiv \mathrm{tr}K_{ij} = g^{ij}K_{ij}, \qquad \tilde{A}_{ij} = e^{-4\phi}\left(K_{ij} - \frac{1}{3}\gamma_{ij}K\right), \tag{2}$$

with $\mathrm{tr}\tilde{A}_{ij} = 0$. Finally, new evolution variables

$$\tilde{\Gamma}^i = \tilde{\gamma}^{jk}\tilde{\Gamma}^i_{jk} \tag{3}$$

are introduced, defined in terms of the Christoffel symbols of the conformal three metric.

The Einstein equations specify a well-known set of evolution equations for the listed variables and are given by

$$(\partial_t - \mathcal{L}_\beta)\tilde{\gamma}_{ij} = -2\alpha\tilde{A}_{ij}, \tag{4}$$

$$(\partial_t - \mathcal{L}_\beta)\phi = -\tfrac{1}{6}\alpha K, \tag{5}$$

$$(\partial_t - \mathcal{L}_\beta)\tilde{A}_{ij} = e^{-4\phi}[-D_iD_j\alpha + \alpha(R_{ij} - 8\pi S_{ij})]^{TF} + \alpha(K\tilde{A}_{ij} - 2\tilde{A}_{ik}\tilde{A}^k_j), \tag{6}$$

$$(\partial_t - \mathcal{L}_\beta)K = -D^iD_i\alpha + \alpha[\tilde{A}_{ij}\tilde{A}^{ij} + \tfrac{1}{3}K^2 + 4\pi(\rho_{\mathrm{ADM}} + S)], \tag{7}$$

$$\partial_t\tilde{\Gamma}^i = \tilde{\gamma}^{jk}\partial_j\partial_k\beta^i + \tfrac{1}{3}\tilde{\gamma}^{ij}\partial_j\partial_k\beta^k + \beta^j\partial_j\tilde{\Gamma}^i - \Gamma^j\partial_j\beta^i + \tfrac{2}{3}\tilde{\Gamma}^i\partial_j\beta^j - 2\tilde{A}^{ij}\partial_j\alpha + 2\alpha(\tilde{\Gamma}^i_{jk}\tilde{A}^{jk} + 6\tilde{A}^{ij}\partial_j\phi - \tfrac{2}{3}\tilde{\gamma}^{ij}\partial_jK - 8\pi\tilde{\gamma}^{ij}S_j), \tag{8}$$

where R_{ij} is the three-dimensional Ricci tensor, D_i the covariant derivative associated with the three metric γ_{ij}, "TF" indicates the trace-free part of tensor objects, and ρ_{ADM}, S_j, and S_{ij} are the matter source terms defined as

$$\rho_{\mathrm{ADM}} \equiv n_\alpha n_\beta T^{\alpha\beta}, \qquad S_i \equiv -\gamma_{i\alpha}n_\beta T^{\alpha\beta}, \qquad S_{ij} \equiv \gamma_{i\alpha}\gamma_{j\beta}T^{\alpha\beta}, \tag{9}$$

where $n_\alpha \equiv (-\alpha, 0, 0, 0)$ is the future-pointing four-vector orthonormal to the spacelike hypersurface and $T^{\alpha\beta}$ is the stress-energy tensor for a perfect fluid [cf. Eq. (19)]. The Einstein equations also lead to a set of physical constraint equations that are satisfied within each spacelike slice,

$$\mathcal{H} \equiv R^{(3)} + K^2 - K_{ij}K^{ij} - 16\pi\rho_{\mathrm{ADM}} = 0, \tag{10}$$

$$\mathcal{M}^i \equiv D_j(K^{ij} - \gamma^{ij}K) - 8\pi S^i = 0, \tag{11}$$

which are usually referred to as Hamiltonian and momentum constraints. Here $R^{(3)} = R_{ij}\gamma^{ij}$ is the Ricci scalar on a three-dimensional time slice. Our specific choice of evolution variables introduces five additional constraints,

$$\det\tilde{\gamma}_{ij} = 1, \tag{12}$$

$$\mathrm{tr}\,\tilde{A}_{ij} = 0, \tag{13}$$

$$\tilde{\Gamma}^i = \tilde{\gamma}^{jk}\tilde{\Gamma}^i_{jk}. \tag{14}$$

Our code actively enforces the algebraic constraints (12) and (13). The remaining constraints, $\mathcal{H}$, $\mathcal{M}^i$, and (14), are not actively enforced and can be used as monitors of the accuracy of our numerical solution. See [59] for a more comprehensive discussion of the these points.

Among the diagnostic quantities, we compute the angular momentum as a volume integral with the expression [60]:

$$J^i_{\mathrm{vol}} = \varepsilon^{ijk}\int_V\left(\frac{1}{8\pi}\tilde{A}_{jk} + x_jS_k + \frac{1}{12\pi}x_jK_{,k} - \frac{1}{16\pi}x_j\tilde{\gamma}^{lm}_{,k}\tilde{A}_{lm}\right)e^{6\phi}d^3x. \tag{15}$$

B. Gauges

We specify the gauge in terms of the standard ADM lapse function α and shift vector β^i [61]. We evolve the lapse according to the "1 + log" slicing condition [62]:

$$\partial_t\alpha - \beta^i\partial_i\alpha = -2\alpha(K - K_0), \tag{16}$$

where K_0 is the initial value of the trace of the extrinsic curvature and equals zero for the maximally sliced initial data we consider here. The shift is evolved using the hyperbolic $\tilde{\Gamma}$-driver condition [59],

$$\partial_t\beta^i - \beta^j\partial_j\beta^i = \tfrac{3}{4}\alpha B^i, \tag{17}$$

$$\partial_t B^i - \beta^j \partial_j B^i = \partial_t \tilde{\Gamma}^i - \beta^j \partial_j \tilde{\Gamma}^i - \eta B^i, \qquad (18)$$

where η is a parameter which acts as a damping coefficient which we set to be constant ($\eta = 1$). The advection terms on the right-hand sides of these equations have been suggested in [63–65].

All the equations discussed above are solved using the CCATIE code, a three-dimensional finite-differencing code based on the Cactus Computational Toolkit [66]. A detailed presentation of the code and of its convergence properties have been recently presented in Ref. [67].

C. Evolution system for the matter

An important feature of the Whisky code is the implementation of a *flux-conservative* formulation of the hydrodynamics equations [68–70], in which the set of conservation equations for the stress-energy tensor $T^{\mu\nu}$ and for the matter current density J^μ, namely

$$\nabla_\mu T^{\mu\nu} = 0, \qquad \nabla_\mu J^\mu = 0, \qquad (19)$$

is written in a hyperbolic, first-order, and flux-conservative form of the type

$$\partial_t \mathbf{q} + \partial_i \mathbf{f}^{(i)}(\mathbf{q}) = \mathbf{s}(\mathbf{q}), \qquad (20)$$

where $\mathbf{f}^{(i)}(\mathbf{q})$ and $\mathbf{s}(\mathbf{q})$ are the flux vectors and source terms, respectively [71]. Note that the right-hand side (the source terms) does not depend on derivatives of the stress-energy tensor. Furthermore, while the system (20) is not strictly hyperbolic, strong hyperbolicity is recovered in a flat spacetime, where $\mathbf{s}(\mathbf{q}) = 0$.

As shown by [69], in order to write system (19) in the form of system (20), the *primitive* hydrodynamical variables (i.e. the rest-mass density ρ, the pressure p measured in the rest-frame of the fluid, the fluid three-velocity v^i measured by a local zero-angular momentum observer, the specific internal energy ϵ, and the Lorentz factor W) are mapped to the so-called *conserved* variables $\mathbf{q} \equiv (D, S^i, \tau)$ via the relations

$$\begin{aligned} D &\equiv \sqrt{\gamma} W \rho, \qquad S^i \equiv \sqrt{\gamma} \rho h W^2 v^i, \\ \tau &\equiv \sqrt{\gamma}(\rho h W^2 - p) - D, \end{aligned} \qquad (21)$$

where $h \equiv 1 + \epsilon + p/\rho$ is the specific enthalpy and $W \equiv (1 - \gamma_{ij} v^i v^j)^{-1/2}$. Note that only five of the seven primitive variables are independent.

In this approach, all variables $\mathbf{q}$ are represented on the numerical grid by cell-integral averages. The functions the $\mathbf{q}$ represent are then *reconstructed* within each cell, usually by piecewise polynomials in a way that preserves conservation of the variables $\mathbf{q}$ [72]. This operation produces two values at each cell boundary which are then used as initial data for the local Riemann problems, whose (approximate) solution gives the fluxes through the cell boundaries. A method-of-lines approach [72], which reduces the partial differential equations (20) to a set of ordinary differential equations that can be evolved using standard numerical methods, such as Runge-Kutta or the iterative Cranck-Nicholson schemes [73,74], is used to update the equations in time (see Ref. [52] for further details). The Whisky code implements several reconstruction methods, such as total-variation-diminishing (TVD) methods, essentially-nonoscillatory (ENO) methods [75], and the piecewise parabolic method (PPM) [76]. Also, a variety of approximate Riemann solvers can be used, starting from the Harten-Lax-van Leer-Einfeldt (HLLE) solver [77], over to the Roe solver [78] and the Marquina flux formula [79] (see [52,53] for a more detailed discussion). A comparison among different numerical methods in our binary-evolution simulations is reported in Appendix A 1.

Note that in order to close the system of equations for the hydrodynamics an EOS which relates the pressure to the rest-mass density and to the energy density must be specified. The code has been written to use any EOS, but all the tests so far have been performed using either an (isentropic) polytropic EOS

$$p = K \rho^\Gamma, \qquad (22)$$

$$e = \rho + \frac{p}{\Gamma - 1}, \qquad (23)$$

or an "ideal-fluid" EOS

$$p = (\Gamma - 1)\rho\epsilon. \qquad (24)$$

Here, e is the energy density in the rest frame of the fluid, K the polytropic constant (not to be confused with the trace of the extrinsic curvature defined earlier), and Γ the adiabatic exponent. In the case of the polytropic EOS (22), $\Gamma = 1 + 1/N$, where N is the polytropic index and the evolution equation for τ does not need to be solved. Note that polytropic EOSs (22) do not allow any transfer of kinetic energy to thermal energy, a process which occurs in physical shocks (shock heating). It is also useful to stress that by being isentropic, the polytropic EOS (22), far from being realistic, can be considered as unrealistic for describing the merger and the post-merger evolution. However, it is used here because it provides three important advantages. First, it provides one "extreme" of the possible binary evolution by being perfectly adiabatic. Second, it allows us to use the same initial data but to evolve it with two different EOS. This is a unique possibility which is not offered by other (more realistic) EOSs. As we will comment below, it has allowed us to highlight subtle properties of the binary dynamics during the inspiral which were not reported before (see the discussion in Sec. III C). Finally, by being isentropic it provides the most realistic description of the inspiral phase, during which the neutron stars are expected to interact only between themselves and only gravitationally.

TABLE I. Properties of the initial data: proper separation between the centers of the stars $d/M_{\rm ADM}$; baryon mass M_b of each star in solar masses; total ADM mass $M_{\rm ADM}$ in solar masses, as measured on the finite-difference grid; total ADM mass $\tilde{M}_{\rm ADM}$ in solar masses, as provided by the Meudon initial data; angular momentum J, as measured on the finite-difference grid; angular momentum $\tilde{J}$, as provided by the Meudon initial data; initial orbital angular velocity Ω_0; mean coordinate equatorial radius of each star r_e along the line connecting the two stars; ratio $r_{e'}/r_e$ of the equatorial coordinate radius of a star in the direction orthogonal to the line connecting the two stars and r_e; ratio of the polar to the equatorial coordinate radius of each star r_p/r_e; maximum rest-mass density of a star $\rho_{\rm max}$. The initial data for the evolutions with polytropic and ideal-fluid EOS are the same. Note that the asterisk in the model denomination will be replaced by "P" or by "IF" according to whether the binary is evolved using a polytropic or an ideal-fluid EOS.

Model	$d/M_{\rm ADM}$	M_b ($M_\odot$)	$M_{\rm ADM}$ ($M_\odot$)	$\tilde{M}_{\rm ADM}$ ($M_\odot$)	J (gcm^2/s)	$\tilde{J}$ (gcm^2/s)	Ω_0 (rad/ms)	r_e (km)	$r_{e'}/r_e$	r_p/r_e	$\rho_{\rm max}$ (g/cm^3)
1.46-45-*	14.3	1.456	2.681	2.694	6.5077×10^{49}	6.5075×10^{49}	1.78	15	0.890	0.899	4.58×10^{14}
1.62-45-*	12.2	1.625	2.982	2.998	7.7833×10^{49}	7.7795×10^{49}	1.85	14	0.923	0.931	5.91×10^{14}
1.62-60-*	16.8	1.625	2.987	3.005	8.5548×10^{49}	8.5546×10^{49}	1.24	13	0.972	0.977	5.93×10^{14}

In contrast to the polytropic EOS, when using the ideal-fluid EOS (24), nonisentropic changes can take place in the fluid and the evolution equation for τ needs to be solved.

D. Adaptive mesh refinement and singularity handling

We use the `Carpet` code that implements a vertex-centered adaptive-mesh-refinement scheme adopting nested grids [80] with a 2:1 refinement factor for successive grid levels. We center the highest resolution level around the peak in the rest-mass density of each star. This represents our rather basic form of AMR.

The time step on each grid is set by the Courant condition (expressed in terms of the speed of light) and so by the spatial grid resolution for that level; the typical Courant coefficient is set to be 0.35. The time evolution is carried out using third-order accurate Runge-Kutta integration steps. Boundary data for finer grids are calculated with spatial prolongation operators employing third-order polynomials and with prolongation in time employing second-order polynomials. The latter allows a significant memory saving, requiring only three time levels to be stored, with little loss of accuracy due to the long dynamical time scale relative to the typical grid time step.

In the results presented below we have used six levels of mesh refinement with the finest grid resolution of $h = 0.12M_\odot = 0.177$ km and the wave-zone grid resolution of $h = 3.84M_\odot = 5.67$ km. Our finest grid has then a resolution of a factor of 2 higher compared to the one used in [44], where a uniform grid with $h = 0.4$ km was instead used. Each star is covered with two of the finest grids, so that the high-density regions of the stars are tracked with the highest resolution available. These "boxes" are then moved by tracking the position of the rest-mass density as the stars orbit and are merged when they overlap. In addition, a set of refined but fixed grids is set up at the center of the computational domain so as to capture the details of the Kelvin-Helmholtz instability (cf. Sec. III E). The finest of these grids extends to $r = 7.5M_\odot = 11$ km. A single grid resolution covers then the region between $r = 150M_\odot = 221.5$ km and $r = 250M_\odot = 369.2$ km, in which our wave extraction is carried out. A reflection symmetry condition across the $z = 0$ plane and a π-symmetry condition[1] across the $x = 0$ plane are used.

We have performed extensive tests to ensure that both the hierarchy of the refinement levels described above and the resolutions used yield results that are numerically consistent although not always in a convergent regime. The initial data used for these tests refer to a binary evolved with an ideal-fluid EOS from an initial separation of 45 km and in which each star has a mass of $1.8M_\odot$; such a mass is larger than the one used for the rest of our analysis (cf. Table I) and it has been employed because it leads to a prompter formation of a black hole, thus saving computational costs.

The 2-norm of the typical violation of the Hamiltonian constraint grows from $\lesssim 10^{-6}$ at the beginning of the simulations to $\lesssim 10^{-4}$ at the end of the simulations. The convergence rate measured in the 2-norm of the violation of the Hamiltonian constraint is $\simeq 1.7$ before the merger (i.e. the same convergence rate measured in the evolution of isolated stars [53]), but it then drops to $\simeq 1.2$ during the merger. It is still unclear whether this difference is due to the generation of a turbulent regime at the merger (see the discussion in Sec. III E and in Ref. [81]) or to a resolution which is close but not yet in a fully convergent regime. Tests showing the convergence rate, the conservation of the mass (baryonic and gravitational), and angular momentum, as well as the consistency in the gravitational waves have been validated by the referee but, for compactness, are not reported here.

The apparent horizon (AH) formed during the simulation is located every few time steps during the evolution [82]. Exploiting a technique we have first developed when

[1]Stated differently, we evolve only the region $\{x > 0, z > 0\}$ applying a 180-degrees rotational-symmetry boundary condition across the plane at $x = 0$.

performing simulations of gravitational collapse to rotating BHs [83,84] and that has now been widely adopted by other codes, we do not make use of the excision technique [85]. Rather, we add a small amount of dissipation to the evolution equations for the metric and gauge variables only and rely on the singularity-avoiding gauge (16) to extend the simulations well past the formation of the AH (note that no dissipation is added to the evolution of matter variables). More specifically, we use an artificial dissipation of the Kreiss-Oliger type [86] on the right-hand sides of the evolution equations for the spacetime variables and the gauge quantities. This is needed mostly because all the field variables develop very steep gradients in the region inside the AH. Under these conditions, small high-frequency oscillations (either produced by finite-differencing errors or by small reflections across the refinement or outer boundaries) can easily be amplified, leave the region inside the AH and rapidly destroy the solution. In practice, for any time-evolved quantity u, the right-hand side of the corresponding evolution equation is modified with the introduction of a term of the type $\mathcal{L}_{\rm diss}(u) = -\varepsilon h^3 \partial_i^4 u$, where h is the grid spacing and $\varepsilon = 0.075$ and is kept constant in space (see Ref. [84] for additional information and different prescriptions).

E. Initial data

As initial data for relativistic-star binary simulations we use the ones produced by the group working at the Observatoire de Paris-Meudon [20,25]. These data, which we refer to also as the ''Meudon data,'' are obtained under the simplifying assumptions of quasiequilibrium and of conformally flat spatial metric. The initial data used in the simulations shown here were produced with the additional assumption of irrotationality of the fluid flow, i.e. the condition in which the spins of the stars and the orbital motion are not locked; instead, they are defined so as to have vanishing vorticity. Initial data obtained with the alternative assumption of rigid rotation were not used because, differently from what happens for binaries consisting of ordinary stars, relativistic-star binaries are not thought to achieve synchronization (or corotation) in the time scale of the coalescence [87]. The Meudon initial configurations are computed using a multidomain spectral-method code, LORENE, which is publicly available [88]. A specific routine is used to transform the solution from spherical coordinates to a Cartesian grid of the desired dimensions and shape.

The binaries used as initial-data configurations have been chosen so as to provide the variety of behaviors that we wanted to illustrate and some of their physical quantities are reported in Table I. Furthermore, since it is the least computationally expensive, we have chosen model 1.62-45-* as our fiducial initial configuration. For this binary the initial coordinate distance between stellar centers in terms of the initial gravitational wavelength is $d = 0.09\lambda_{\rm GW}$, where $\lambda_{\rm GW} = \pi/\Omega_0$ is the gravitational wavelength for a Newtonian binary of orbital angular frequency Ω_0. For evolutions that employ a polytropic EOS, the polytropic exponent is $\Gamma = 2$ and the polytropic coefficient $K = 123.6 = 1.798 \times 10^5$ g^{-1} cm^5 s^{-2}. (Reference [4] has recently made the useful remark that a choice of $\Gamma = 2.75$ and $K = 30\,000$ leads to an EOS that fits well the supernuclear regime of the Shen-EOS at zero temperature [89], as well as yielding density profiles that are very similar to those obtained with that realistic EOS; unfortunately no initial data with this adiabatic exponent is available at the moment.)

III. BINARY DYNAMICS

In what follows we describe the matter dynamics of the binary initial data discussed in the previous section. To limit the discussion and highlight some of the most salient aspects we will consider two main classes of initial data, represented by models 1.62-45-* and 1.46-45-*, respectively. These models differ only in the rest mass, the first one being composed of stars each having a mass of $1.625M_\odot$ (which we refer to as the *high-mass* binaries), while the second one is composed of stars of mass $1.456M_\odot$ (which we refer to as the *low-mass* binaries).

Variations of these initial data will also be considered by changing, for instance, either the initial coordinate separation (i.e. 60 km in place of 45 km) or the EOS (i.e. an ideal-fluid EOS or a polytropic one). Additional variations involving, for instance, different mass ratios, will be presented elsewhere [90].

A. Polytropic EOS: high-mass binary

We start by considering the evolution of the high-mass binary evolved with the polytropic EOS, i.e. model 1.62-45-P in Table I. Figure 1, in particular, collects some representative isodensity contours (i.e. contours of equal rest-mass density) on the (x, y) (equatorial) plane, with the time stamp being shown on the top of each panel and with the color-coding bar being shown on the right in units of g/cm^3.

The binary has an initial coordinate separation between the maxima in the rest-mass density of 45 km and, as we will discuss more in detail later on, a certain amount of coordinate eccentricity and tidal coordinate deformation is introduced by the initial choice for the shift vector. As the stars inspiral, their orbital angular velocity increases and after about 2.2 orbits, or equivalently after about 5.3 ms from the beginning of the simulation, they merge, producing an object which has a mass well above the maximum one for uniformly rotating stars, but which supports itself against gravitational collapse by a large differential rotation. Such an object is usually referred to as a hypermas-

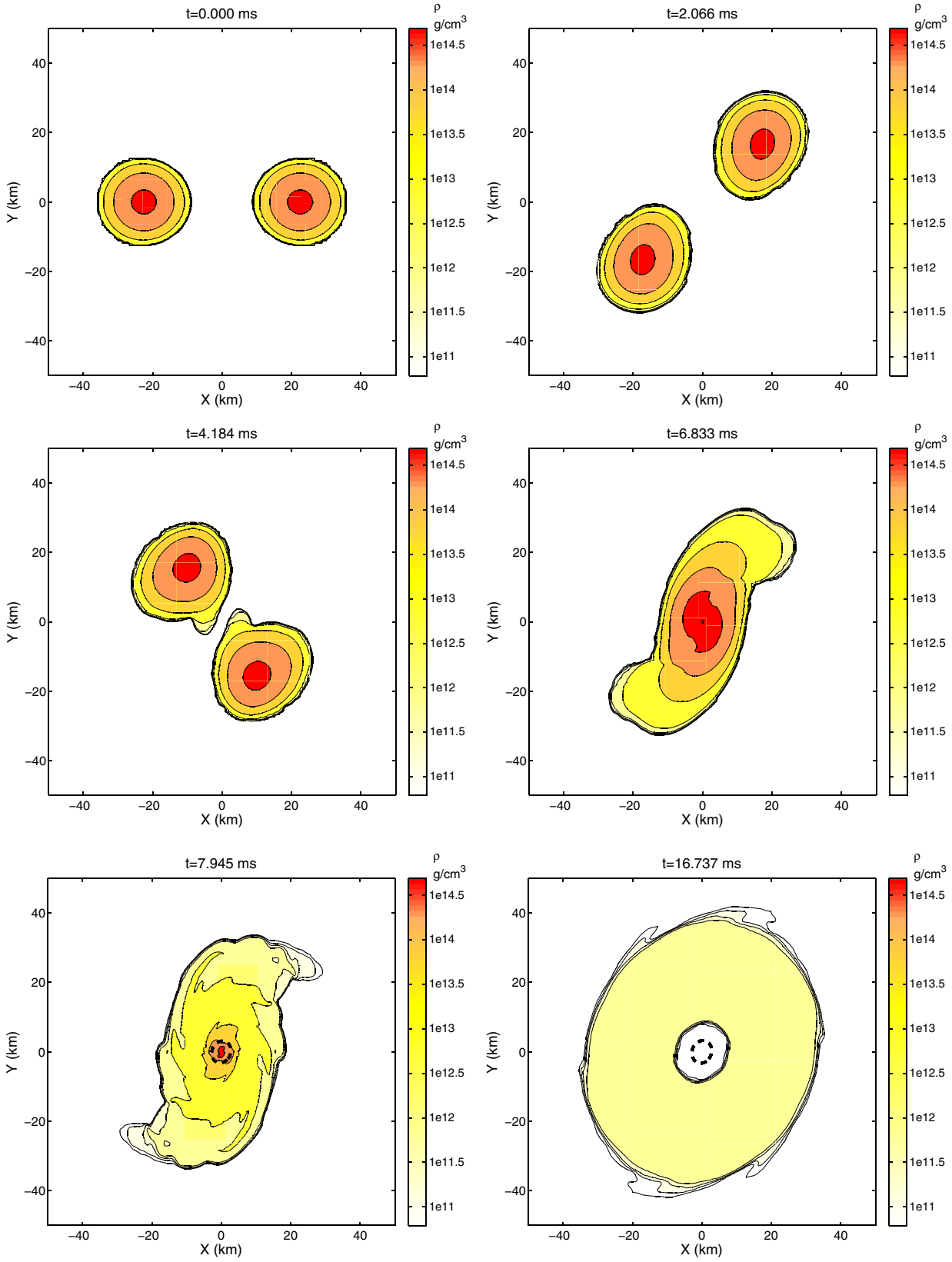

FIG. 1 (color online). Isodensity contours on the (x, y) (equatorial) plane for the evolution of the high-mass binary with the polytropic EOS (i.e. model 1.62-45-P in Table I). The time stamp in ms is shown on the top of each panel, the color-coding bar is shown on the right in units of g/cm^3, and the thick dashed line represents the AH.

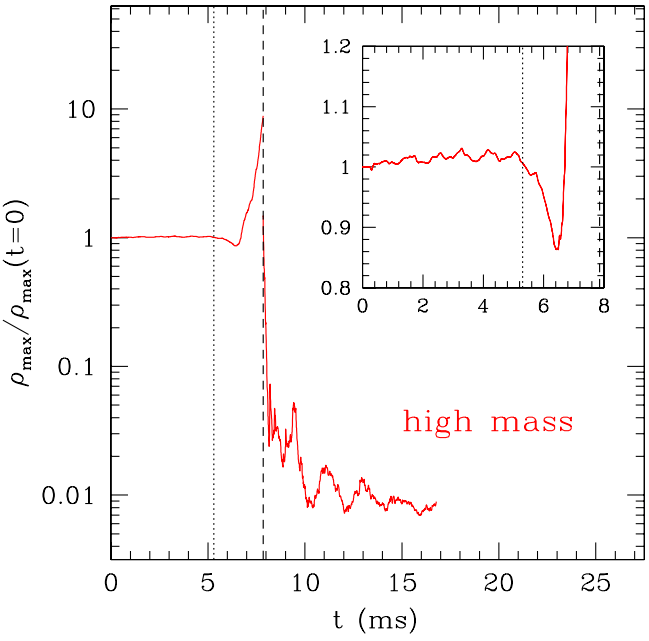

FIG. 2 (color online). Evolution of the maximum rest-mass density normalized to its initial value for the high-mass binary. Indicated with a dotted vertical line is the time at which the stars merge, while a vertical dashed line shows the time at which an AH is first found and which is a few ms only after the merger in this case. After this time, the maximum rest-mass density is computed in a region outside the AH and therefore it refers to the density of the oscillating torus. It is only a few orders of magnitude smaller. Note that the non-normalized value of the maximum rest-mass density at $t = 0$ is $5.91 \times 10^{14}\mathrm{g/cm}^3$ (see Table I). The binary has been evolved using the polytropic EOS.

sive neutron star or HMNS.[2] As the inspiral proceeds and the two NSs progressively approach each other, tidal waves produced by the tidal interaction become visible (cf. first and second rows of panels in Fig. 1) and these are particularly large, i.e. of ~5%, for the high-mass binary and considerably smaller for the low-mass one (cf. Fig. 8).

This is shown in Fig. 2, which reports the evolution of the maximum rest-mass density normalized to its initial value. Indicated with a dotted vertical line is the time at which the stars merge (which we define as the time at which the outer layers of the stars enter in contact), while a vertical dashed line shows the time at which an AH is found. After this time the maximum rest-mass density is computed in a region outside the AH and therefore it refers to the density of the oscillating torus. It is only a few orders of magnitude smaller. Note that before the merger the central rest-mass density not only oscillates but it also increases secularly, although at a much smaller rate (cf. also Fig. 6).

As mentioned above, the merger takes place after about 5 ms and the two NSs collide with a rather large impact parameter. This reduces significantly the strength of the shocks which have been computed in the case of head-on collisions [91], but it also produces a considerable amount of shear, which could then lead to a series of interesting dynamical instabilities (see also the discussion in Sec. III E). Because of the adiabatic nature of the EOS, which prevents the formation of physical shocks (i.e. discontinuities where entropy is increased locally),[3] the HMNS produced at the merger is beyond the stability limit for gravitational collapse, so that despite the high amount of angular momentum and the large degree of differential rotation,[4] it rapidly collapses to produce a rotating BH, at about 8 ms.

More specifically, soon after the merger, the two massive and high-density cores of the NSs coalesce and during this rapid infall they experience a considerable decompression of ~15% or more as shown in the small inset of Fig. 2. However, after $t \sim 6$ ms, the maximum rest-mass density is seen to increase exponentially, a clear indication of the onset of a quasiradial dynamical instability, and this continues through the formation of an AH, which is first found at time $t = 7.85$ ms (see the last row of panels in Fig. 1 where the AH is shown with a thick dashed line, or Fig. 2, where the time of appearance is marked by a dashed vertical line).

This complex general behavior, namely, the very small secular increase in the central rest-mass density accompanied by small tidal oscillations, and the final decompression as the two NS cores merge into one, should help to clarify a long-standing debate on whether the NSs experience a compression prior to the merger which leads them to collapse to a BH [34,35,92] or, rather, a decompression [17,93,94], as a result of the dynamical instability leading to the merger. Clearly, for the rather restricted set of stellar models which are close to the stability limit to BH collapse, the small secular increase could lead to the formation of two BHs prior to the merger.

After an AH is first found, the amount of matter outside of it is still quite large and, most importantly, it is the one with the largest amount of angular momentum. This leads

[2]We recall that a HMNS is a star whose mass is larger than the maximum one allowed for a uniformly rotating model with the same EOS (i.e. the supramassive limit). For the $\Gamma = 2$ polytropes considered here this maximum mass is $M = 2.324M_\odot$ (with an equivalent baryon mass of $M_b = 2.559M_\odot$), while the maximum mass for a nonrotating model is $M = 2.027M_\odot$ (with an equivalent baryon mass of $M_b = 2.225M_\odot$). Clearly, all the models considered in Table I lead to a HMNS after the merger.

[3]Note that very large gradients can nevertheless be produced because of the nonlinear nature of the hydrodynamic equations. These gradients, however, are not physical shocks in that no entropy is increased locally.

[4]Note that the HMNS is not axisymmetric and hence it is difficult to provide a unique measure of the degree of differential rotation. On average, however, the angular velocity decreases about 1 order of magnitude between the rotation axis and the surface.

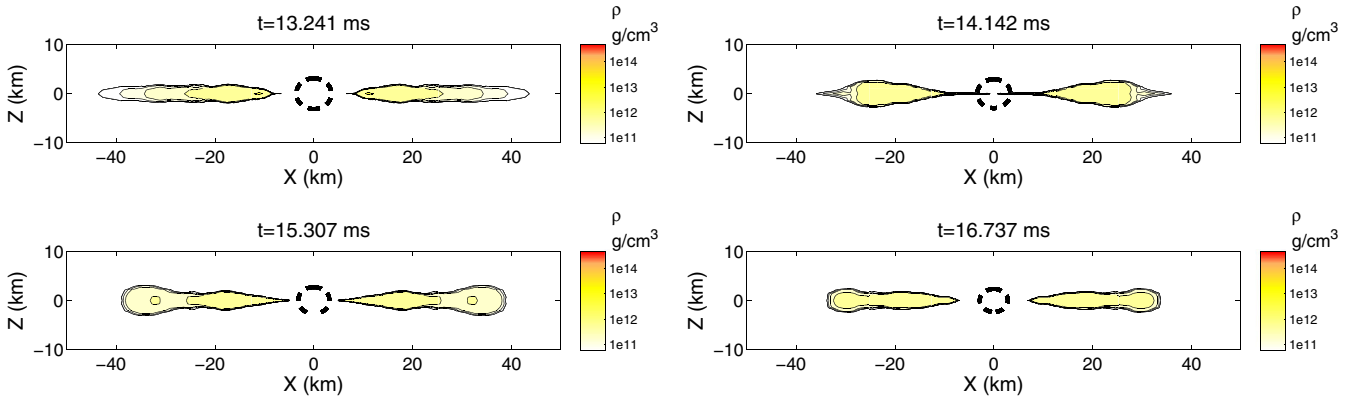

FIG. 3 (color online). Isodensity contours on the (x, z) plane highlighting the formation of a torus surrounding the central BH, whose AH is indicated with a thick dashed line. The data refers to the high-mass binary evolved with the polytropic EOS.

to the formation of an accretion torus with an average density between 10^{12} and 10^{13} g/cm^3, a vertical size of a few km but a horizontal one between 20 and 30 km (see evolution of $\rho_{\max}$ in Fig. 2 after the AH). The torus has an *initial* rest mass of $(M_{\rm T})_0 \simeq 0.04 M_\odot$,[5] which, however, decreases rapidly to become $(M_{\rm T})_{3\ {\rm ms}} = 0.0117 M_\odot$ only 3 ms later.

The dynamics of the torus are summarized in Fig. 3, which shows the isodensity contours on the (x, z) plane; also in this case the time stamp is shown on the top of each panel, while the color-coding bar is shown on the right in units of g/cm^3. Note that the panels refer to times between 13.2 ms and 16.7 ms and thus to a stage in the evolution which is between the last two panels of Fig. 1. Other information on the properties of the merged object can be found in Table II.

Overall, the torus has a dominant $m = 0$ (axisymmetric) structure but, because of its violent birth, it is very far from an equilibrium. As a result, it is subject to large oscillations, mostly in the radial direction, as it tries to compensate between the excess angular momentum and the intense gravitational field produced by the BH. In doing so, it triggers quasiperiodic oscillations with a period of $\sim$2 ms, during which the torus moves in towards the BH, accreting part of its mass. A behavior very similar to this one has been studied in detail in a number of related works [95–99], in which the torus was treated as a test fluid. While the above-mentioned studies represent an idealization of the dynamics simulated here, they have highlighted that the harmonic dynamics of the torus represent a generic response of the fluid to a quasiradial oscillation with a frequency reminiscent of the epicyclic frequency for point-like particles in a gravitational field [100,101]. Furthermore, because of the large quadrupole moment possessed by the torus and its large variations produced by the oscillations, a non-negligible amount of gravitational radiation can be produced as a result of this process (see also the discussion of Fig. 18).

As mentioned in the introduction, the existence of a massive torus around the newly formed rotating BH is a key ingredient in the modeling of short GRBs and the ability of reproducing this feature through a fully nonlinear simulation starting from consistent initial data is a measure of the maturity of simulations of this type. For compactness, we cannot present here a detailed study of the dynamics of the torus, of the variation of its mass, and of the consequent accretion onto the BH. Such an analysis will be presented elsewhere [90], but it is sufficient to remark here that the choice of suitable gauge conditions and the use of artificial viscosity for the field variables allow for a stable evolution of the system well past BH formation and for all of the time we could afford computationally.

Using the isolated-horizon formalism [102] and its numerical implementation discussed in Ref. [103], we have measured the final BH to have a mass $M_{\rm BH} = 2.99 M_\odot$ and spin $J_{\rm BH} = 7.3 M_\odot^2 = 6.4 \times 10^{49}$ g cm^2 s^{-1}, thus with a dimensionless spin $a \equiv J_{\rm BH}/M_{\rm BH}^2 = 0.82$ (cf. Table II). This is a rather surprising result when compared to the equivalent measure made in the inspiral and merger of an equal-mass binary BH. In that case, it has been found that the final dimensionless spin is $a_{\rm fin} \simeq 0.68$ for BHs that are initially nonspinning and increasing/decreasing for BHs that have spins parallel/antiparallel with the orbital angular momentum (see, e.g., [104–107]). More specifically, the two initial BHs need to have a substantial spin, with $a_{\rm initial} \simeq 0.45$, in order to produce a final BH with $a_{\rm final} \simeq 0.82$. On the other hand, the NSs have here little initial spin

[5]We define the initial mass of the torus as the rest mass outside the AH soon after the AH is first found. Note that such a measure could be ambiguous since the time of the first AH detection depends also on the frequency with which the AH has been searched for and on the initial guess for the AH radius. To improve this notion and to give a measure that is indicatively comparable for different simulations, we take the values of the rest mass of the torus at the time at which the AH mean radius has reached the arbitrarily chosen value of 2.1. This mass should really be taken as an upper limit for the torus rest mass, since its value decreases considerably as the evolution proceeds and the torus accretes onto the BH.

TABLE II. Summary of the results of the simulations: proper separation between the centers of the stars $d/M_{\rm ADM}$; baryon mass M_b of each star in solar masses; initial rest mass of the torus $(M_{\rm T})_0$ (see footnote on page 10); rest mass of the torus 3 ms after the appearance of the AH $(M_{\rm T})_{3\ {\rm ms}}$ (actually 3 ms after the time when the AH mean radius has reached the value 2.1, see footnote on page 10); mass of the BH $M_{\rm BH}^{\rm IH}$, as computed in the isolated-horizon formalism; angular momentum of the BH $J_{\rm BH}^{\rm IH}$, as computed in the isolated-horizon formalism; BH spin parameter $a^{\rm IH} \equiv (J_{\rm BH}/M_{\rm BH}^2)^{\rm IH}$, as computed in the isolated-horizon formalism; ratio of the ADM mass carried by the waves to the initial ADM mass; ratio of the angular momentum carried by the gravitational waves to the initial angular momentum.

Model	$d/M_{\rm ADM}$	$M_b/M_\odot$	$(M_{\rm T})_0/M_\odot$	$(M_{\rm T})_{3\ {\rm ms}}/M_\odot$	$M_{\rm BH}^{\rm IH}/M_\odot$	$J_{\rm BH}^{\rm IH}$ (g cm^2/s)	$a^{\rm IH}$	$M_{\rm GW}/M_\odot$	$J_{\rm GW}/J(t=0)$
1.46-45-P	14.3	1.456	0.1	0.0787	2.60	4.61×10^{49}	0.76	1.8×10^{-2}	0.21
1.62-60-P	16.8	1.625	0.04	0.00115	3.11	7.0×10^{49}	0.82	9.6×10^{-3}	0.22
1.62-45-P	12.2	1.625	0.04	0.0117	2.99	6.4×10^{49}	0.82	9.3×10^{-3}	0.12
1.46-45-IF	14.3	1.456	...	...	...	...	...	8.5×10^{-3}	0.15
1.62-45-IF	12.2	1.625	0.2	0.0726	2.94	6.4×10^{49}	0.84	1.2×10^{-2}	0.17

(they are essentially spherical besides the tidal deformation) and the little they have is antiparallel to the orbital angular momentum (i.e. they counterspin with respect to the orbital angular momentum). Yet, they are able to produce a rapidly spinning BH. It is apparent therefore that the merger of two equal-mass NSs is considerably less efficient in losing the orbital angular momentum (or equivalently more efficient in transferring the orbital angular momentum to the final BH), thus producing a BH which is comparatively more rapidly spinning.

An important validation of the accuracy of the simulations presented here can be appreciated when comparing the evolution of the same binary when evolved starting from different initial separations. More specifically, we have considered high-mass binaries with initial coordinate separation of either 45 or 60 km (i.e. models 1.62-45-P and 1.62-60-P in Table I) and evolved them with a polytropic EOS. The results of this verification are summarized in Fig. 4, with the upper part reporting the evolution of the proper separation (continuous lines) and the lower one that of the coordinate separation (dotted lines) for binaries with initial coordinate separation of either 45 or 60 km (i.e. models 1.62-45-P and 1.62-60-P in Table I). It should be remarked that the evolution of the latter binary is computationally much more challenging, with an inspiral phase that is about three times as long when compared with the small-separation binary. In particular, the stars merge at $t \sim$ 18 ms, corresponding to $\sim$5.5 orbits. This is to be compared with the $\sim$2.2 orbits of 1.62-45-P and it is close to the limit of what is computationally feasible at these resolutions.

The first thing to note in Fig. 4 is the remarkable difference between the coordinate separation, which shows very large oscillations, and the proper separation, which instead shows only very little variations superposed to the secular decrease. These are probably associated to a small but nonzero residual eccentricity like the one observed in binary BH simulations [67]. The oscillations in the coordinate separation, which have been reported also in Ref. [45] (cf. their Figs. 5 and 7), are in our case clearly related to the gauge choice, as demonstrated by the evolution of the proper separation. This is also apparent when looking at Fig. 5, which shows the coordinate trajectory (dashed line) and the proper trajectory (solid line) of one of the two NSs in the high-mass binary starting from a coordinate separation of 45 km. While a certain amount of eccentricity is present also in the proper trajectory, this is rather small.

A more careful analysis has revealed that the large oscillations in the coordinate separation are simply the result of nonoptimal gauge conditions. As mentioned in Sec. II E, we import the initial data from the solution of the Meudon group, adopting the same shift vector β^i com-

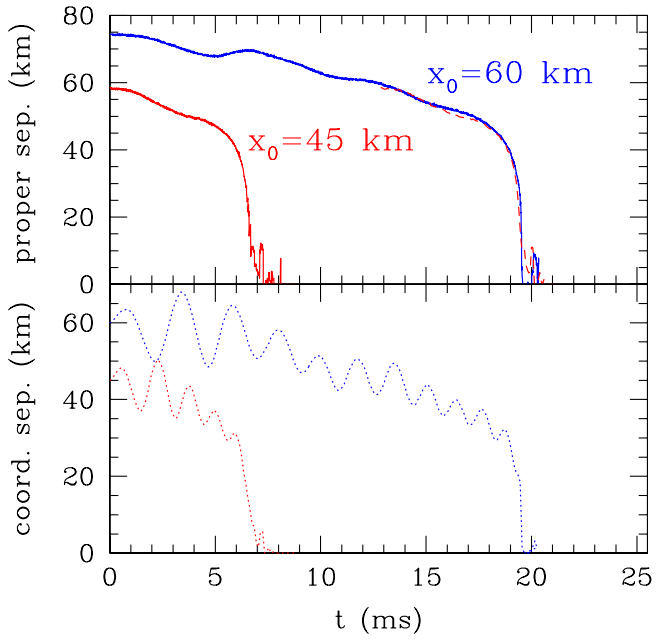

FIG. 4 (color online). Evolution of the proper separation (top part) and of the coordinate separation (bottom part) for binaries with initial coordinate separation of either 45 or 60 km (i.e. models 1.62-45-P and 1.62-60-P in Table I). Indicated with a dashed line is the proper separation for the binary starting at 45 km and suitably shifted in time.

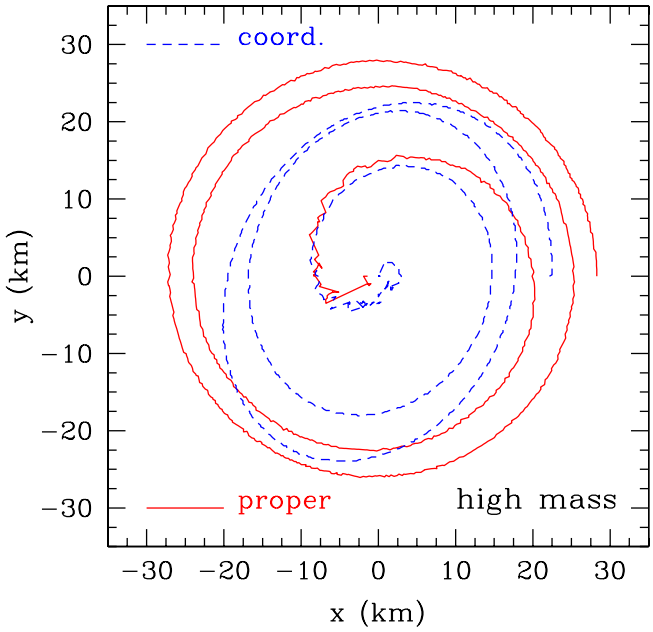

FIG. 5 (color online). Coordinate (dashed line) and proper (solid line) trajectory of one of the stars for the high-mass binary from a coordinate distance of 45 km (about 2.2 orbits).

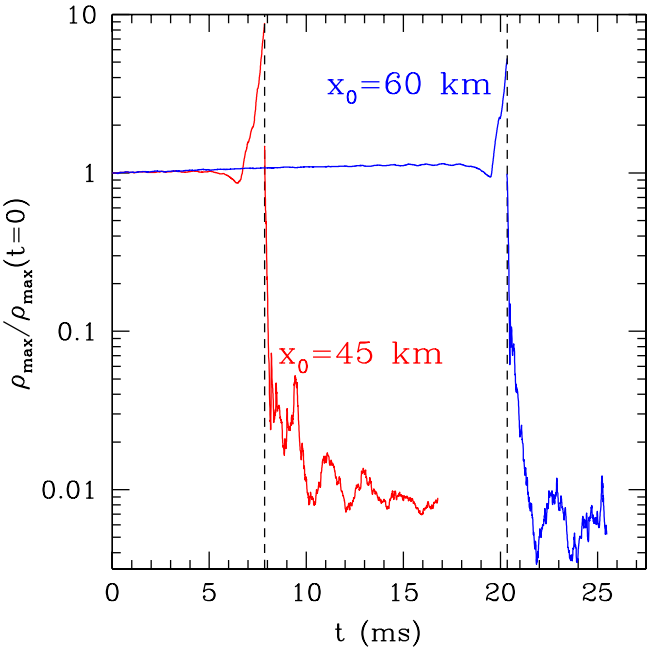

FIG. 6 (color online). Evolution of the maximum rest-mass density normalized to its initial value for high-mass binaries with initial coordinate separation of either 45 or 60 km. The vertical dashed lines denote the time at which an AH was found. The polytropic EOS was used for the evolutions.

puted for the quasicircular solution. While this may seem like a reasonable thing to do, it actually introduces the oscillations commented above. We have also performed alternative simulations in which the shift vector has been set to be zero initially and then evolved with the gauge conditions (17). We have found that in this case also the coordinate separation is much better behaved and only very small oscillations are present (see also the discussion in Appendix A 2).

When concentrating on the evolution of the proper separation it is clear that the binary starting at a large separation has a larger eccentricity, but also that most of it is lost by the time the stars merge. Indicated with a dashed line in Fig. 4 is also the evolution of the proper separation for the binary starting at 45 km when this is suitably shifted in time of ~13 ms; the very good overlap between the two curves is what one expects for a binary system that is simply translated in time and it gives a measure of our ability of accurately evolving binary NSs for a large number of orbits. This provides us with sufficiently long waveforms to perform a first match with the PN expectations and also to establish the role played by the tidal interaction between the two NSs as they inspiral. Both of these studies will be presented elsewhere [90].

A comparison of the waveforms produced in these two simulations will be discussed in Sec. IVA, but we show in Fig. 6 the evolution of the maximum rest-mass density normalized to its initial value for high-mass binaries with initial coordinate separation of either 45 or 60 km. For the large-separation binary, we observe a behavior very similar to that of the small-separation binary, as discussed for Fig. 2, namely, the very small secular increase with superposed small tidal oscillations, the decompression as the two NS cores merge and the final exponential growth produced by the collapse to a BH. Note, however, that the two evolutions are not exactly the same and that small differences are appreciable both in the decompression phase and in the post-collapse phase which is dominated by the dynamics of the torus around the BH (note that the different final values in $\rho_{\max}$ are due to the different times at which the AH is first found and which do not coincide for the two runs; see also the footnote on page 10).

Although a larger truncation error is to be expected in the case of the large-separation binary simply because of the larger integration time, we believe these differences are genuine and reflect the fact that the initial data used are not invariant under time translation. Stated differently, the large-separation binary 1.62-60-P, when evolved down to a separation of 45 km, will not coincide with the equilibrium solution 1.62-45-P computed for a quasicircular binary in equilibrium at 45 km. Because these differences are mostly in the internal structure, the deviations in the evolution become evident only at and after the merger and are essentially absent in the premerger evolution of both the central-density (cf. Fig. 6) and of the waveforms (cf. Fig. 20 in Sec. IVA).

Since considerations of this type have never been made before in the literature and we are not aware of careful comparative studies of this type, our conclusions require further validation. Work is now in progress to perform

similar simulations with different polytropic indices. If the differences reported in Fig. 6 are indeed physical, they will also show variations in case stiffer or softer EOS are considered and they should indeed disappear for perfectly incompressible stars. The results of this analysis will be reported in a future work [90].

B. Polytropic EOS: low-mass binary

We next consider the evolution of the low-mass binary evolved with the polytropic EOS, i.e. model 1.46-45-P in Table I. As for the high-mass binary, we first show in Fig. 7, the representative isodensity contours on the (x, y) plane, with the time stamp being shown on the top of each panel and with the color-coding bar being shown on the right in units of g/cm^3. Note that because the evolution is different in this case, the times at which the isodensity contours are shown are different from those in Fig. 1.

Since the mass difference with model 1.62-45-P is less than 10%, one expects that the orbital dynamics *before* the merger are essentially the same. Indeed this is what our simulations indicate and differences appear only as higher-order effects, such as in the strength of the tidal waves (see Fig. 7). However, despite the small difference in mass, the evolution *after* the merger is considerably different. This is nicely summarized in Fig. 8 which shows that the merger time is essentially the same as for the high-mass binary (i.e. ~ 5.3 ms), but the subsequent evolution does not lead to the prompt formation of a BH. Rather, the HMNS is still quite far from the instability threshold and undergoes a number of quasiperiodic oscillations (cf. Fig. 8), which have almost constant amplitude in the central rest-mass density.

A more careful analysis reveals that the core of the HMNS undergoes violent nonaxisymmetric oscillations, with the development of an overall $m = 2$ deformation, i.e. a bar, as the system tries to reach a configuration which is energetically favorable through the rearrangement of the angular-momentum distribution. The bar-deformed star has an initial value of the ratio of the kinetic energy to the binding energy $T/|W| \simeq 0.22$, which remains roughly constant and only slightly decreases to 0.19 until the time of the collapse. As the bar rotates, it also loses large amounts of angular momentum through gravitational radiation and this is reported in Fig. 9, which shows the evolution of the angular momentum as normalized to the initial value. The top panel, in particular, refers to the high-mass binary, while the bottom one to the low-mass binary (a more detailed discussion of the losses of energy and angular momentum will also be presented in Sec. IV C). Indicated with different lines are the computed values of the volume-integrated angular momentum [solid line, computed with the integral (15)], of the angular momentum lost to gravitational waves (dotted line), and of their sum (dashed line). In both cases the slight secular increase is due to the truncation error and is at most of 3% over more than 20 ms (cf. dot-dashed line). A very similar figure can be made for the one of the ADM mass, whose conservation is even higher (the error is below 1%). For compactness we will not show such a figure here.

Note that the loss of angular momentum is of $\sim 5\%$ of the total initial angular momentum during the inspiral and merger, but becomes much larger once the HMNS has been produced and while the bar-deformed core rotates. Indeed, in the case of the large-mass binary this loss increases to $\sim 13\%$ after the BH quasinormal ringing, while it becomes as large as $\sim 22\%$ for the low-mass binary. Overall, the post-merger evolution for the low-mass binary is rather long and spans over ~ 16 ms. The inset in Fig. 8 shows that during this time the maximum rest-mass density oscillates but it also increases secularly of a factor of about 2. This is due to the fact that as the HMNS loses angular momentum, its centrifugal support is also decreased and thus it reaches more and more compact configurations. At one point the HMNS is past the threshold of the quasiradial instability for the collapse to a BH, which takes place at ~ 20 ms (cf. Fig. 8), with an AH being found at $t = 21.3$ ms.

Also in this case, a large amount of matter with sufficient angular momentum is found to be orbiting outside the BH in the form of an accretion disc. Differently from the high-mass binary, however, the torus here has a larger average rest-mass density (between 10^{12} and 10^{14} g/cm^3; see evolution of $\rho_{\max}$ in Fig. 8 after the AH), a larger extension in the equatorial plane (between 20 and 50 km) but a comparable vertical extension (below 10 km). It also has a larger baryon mass, which is initially $(M_{\rm T})_0 = 0.1 M_\odot$ and becomes $(M_{\rm T})_{3\ {\rm ms}} = 0.0787 M_\odot$ after 3 ms (see footnote on page 10 and Table II). The dynamics of the torus are summarized in Fig. 10, which shows the isodensity contours on the (x, z) plane; note that the panels refer to times between 21.4 ms and 27.4 ms and thus to a stage in the evolution which is between the last two panels of Fig. 7. A simple comparison between Figs. 3 and 10 is sufficient to capture the differences between the tori in the two cases and also to highlight that for a polytropic EOS the *high-mass* binary produces a *lower-mass* torus (cf. Table II and see the discussion in Sec. IV C).

In analogy with what is seen for the high-mass binary, the torus has an overall axisymmetric structure and is far from equilibrium. As a result, it is subject to large oscillations, mostly in the radial direction, at a frequency close to the epicyclic one. A more detailed analysis of this will be presented in a companion paper [90].

Using again the isolated-horizon formalism we have estimated that the final BH has in this case a mass $M_{\rm BH} = 2.60 M_\odot$, spin $J_{\rm BH} = 5.24 M_\odot^2 = 4.61 \times 10^{49}\ {\rm g\,cm^2\,s^{-1}}$, and thus a dimensionless spin $a \equiv J_{\rm BH}/M_{\rm BH}^2 = 0.76$ (cf. Table II). Interestingly, the dimensionless spin is lower in the low-mass binary.

It should also be remarked that the long time interval before which the collapse takes place has prevented previous studies from the complete calculation of the dynam-

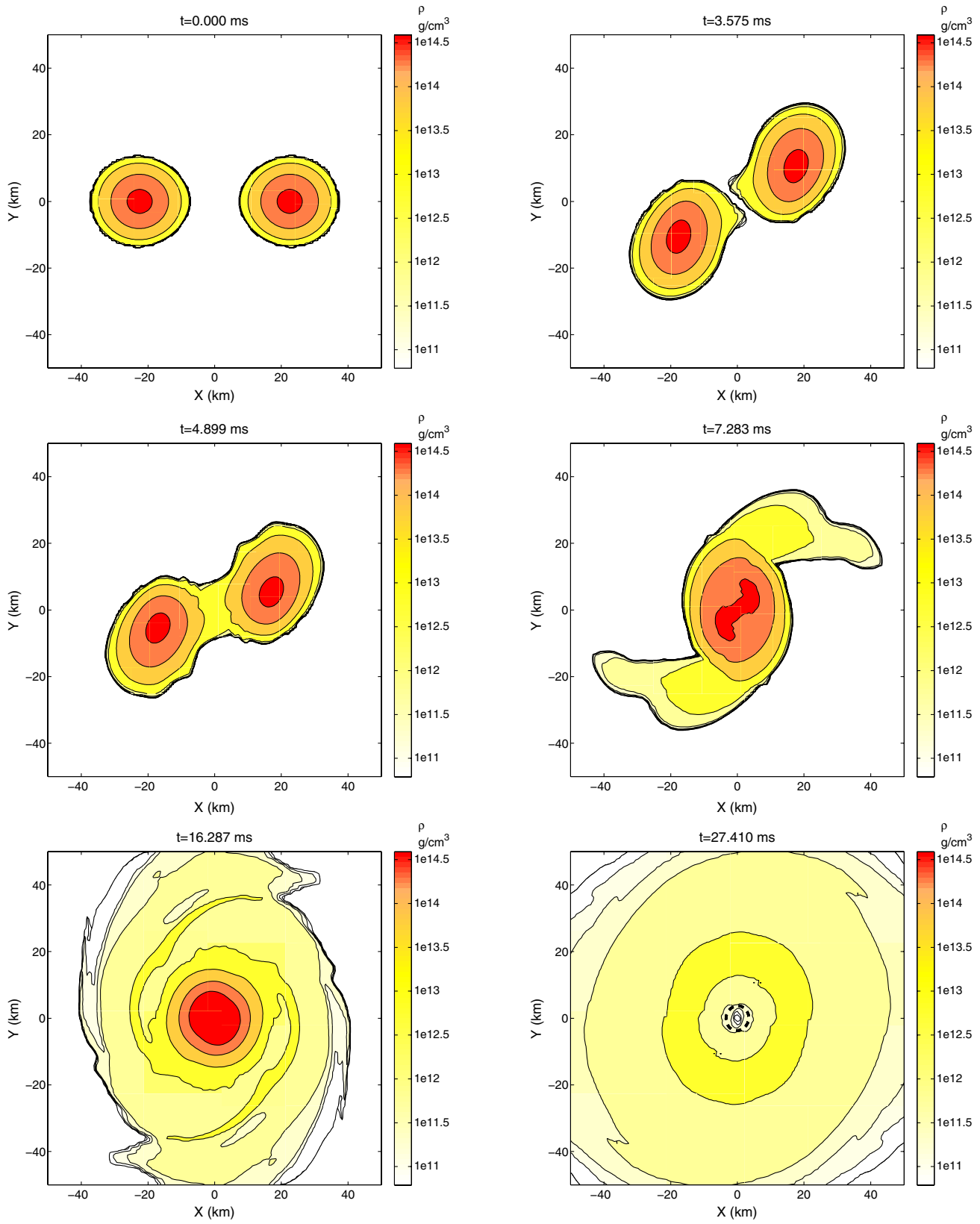

FIG. 7 (color online). Isodensity contours on the (x, y) (equatorial) plane for the evolution of the *low-mass* binary with the *polytropic* EOS (i.e. model 1.46-45-P in Table I). The time stamp in ms is shown on the top of each panel, the color-coding bar is shown on the right in units of g/cm^3, and the thick dashed line represents the AH.

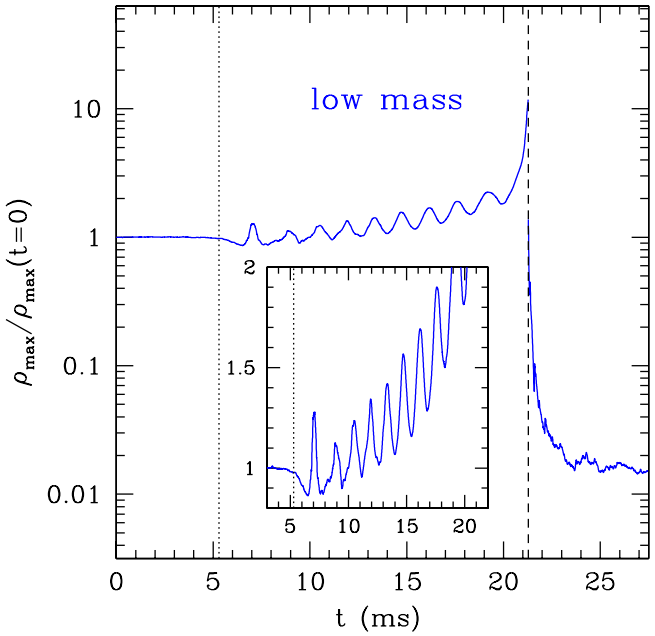

FIG. 8 (color online). The same as in Fig. 2 but for the low-mass binary. Note that the merger time is essentially the same as for the high-mass binary but there is a long delay in the collapse and the onset of quasiharmonic oscillations in the HMNS. The binary has been evolved using the polytropic EOS. Note that the non-normalized value of the maximum rest-mass density at $t = 0$ is 4.58×10^{14} g/cm^3 (see Table I).

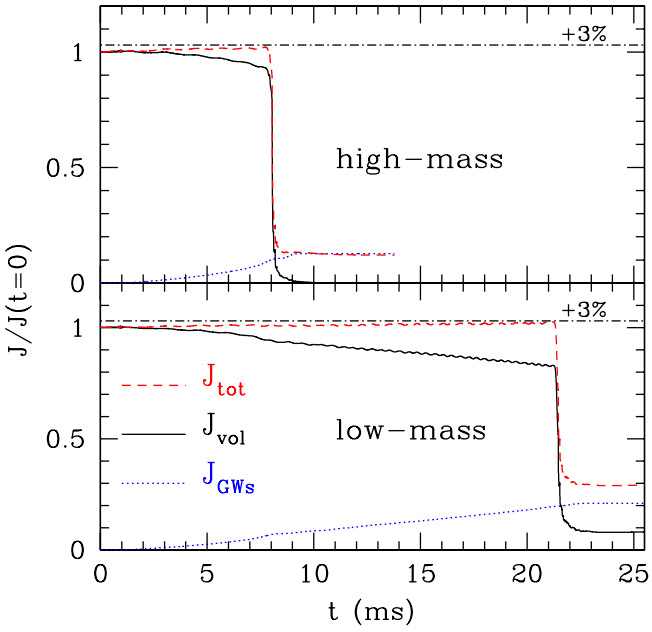

FIG. 9 (color online). Conservation of the total angular momentum for the high-mass binary (upper plot) and the low-mass one (lower plot). Indicated with different lines are the computed values of the volume-integrated angular momentum (solid line), of the angular momentum lost to gravitational waves (dotted line), and of their sum (dashed line). The dot-dashed line marks a 3% error.

ics of NS binaries which would not lead to the *prompt* formation of a BH. The investigations of Refs. [44,45,49], for instance, are limited to a few ms after the merger and should be contrasted with the evolutions reported here that cover a time scale of ~30 ms, also for the additional calculation of the gravitational waves. As a result, our simulations represent, within an idealized treatment of the matter, the first complete description of the inspiral and merger of a NS binary leading to the *delayed* formation of a BH.

C. Ideal-fluid EOS: high-mass binary

We now move on to discussing the dynamics of binary inspiral and merger when the other EOS, the ideal-fluid one in Eq. (24), is used. As discussed in Sec. II C, while this is an idealized and analytic EOS, it has the important property of being nonisentropic and thus of allowing for the change of the thermal part of the internal energy density (or, equivalently, of the temperature). As we will show in the remainder of this section, this difference can lead to significant differences in the properties and dynamics of

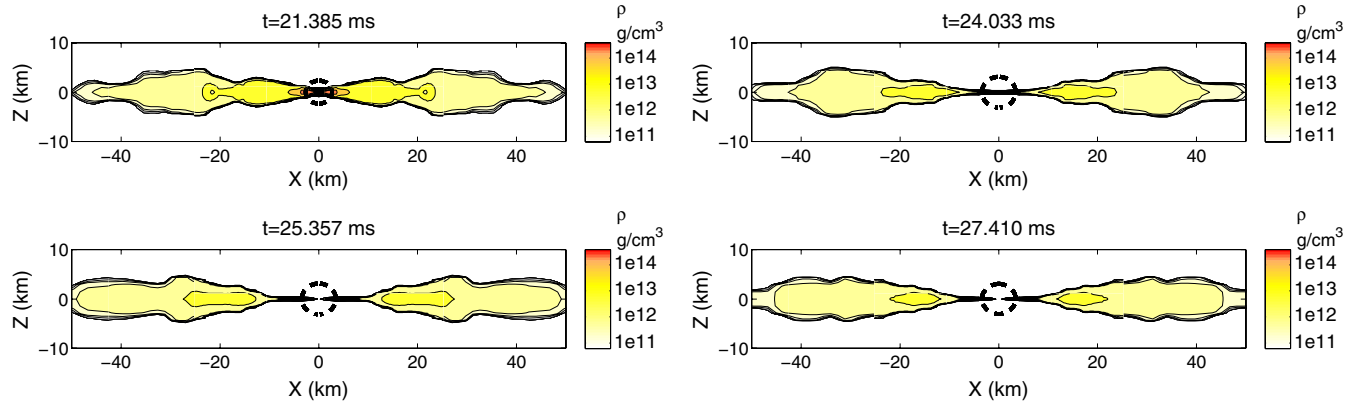

FIG. 10 (color online). Isodensity contours on the (x, z) plane, highlighting the formation of a torus surrounding the central BH, whose AH is indicated with a thick dashed line. The data refers to the low-mass binary evolved with the polytropic EOS (cf. Fig. 3).

the HMNS produced by the merger. More specifically, we concentrate on the evolution of model 1.62-45-IF in Table I, namely, a binary in which each NS has a baryon mass of $M_b = 1.625 M_\odot$ and an initial coordinate separation of 45 km. As for the previous binaries, we collect in Fig. 11 some representative isodensity contours on the equatorial plane.

As one would expect from PN considerations (which suggest that finite-size effects are expected at orders equal or smaller than the fifth [108]), the bulk dynamics of the binary before the merger are essentially identical to the one already discussed for model 1.62-45-P and small differences are appreciable only in the low-density layers of the stars, where the different tidal fields cause comparatively larger amounts of matter to be stripped from the surface; this can be appreciated by comparing the second and third panels of Figs. 1 and 11. Indeed, this is a subtle point which is worth remarking: when using the ideal-fluid EOS, the evolution *before* the merger (i.e. during the inspiral) is not isentropic. This is because small shocks are produced in the very low-density layers of the stars as these orbit. These small shocks channel some of the orbital kinetic energy into internal energy, leading to small ejections of matter (i.e. $\sim 10^{-6} M_\odot$), and are thus responsible for the slight differences in the inspiral. We also note that these shocks would appear quite independently of the fact that the NSs are surrounded by an atmosphere as they represent the evolution of small sound waves that, propagating from the central regions of the stars, steepen as they move outwards; we have checked that essentially identical results are obtained when changing the threshold for the atmosphere of one or more orders of magnitude (a discussion of this process for isolated stars evolved within the Cowling approximation can be found in Ref. [109] and in Ref. [110] for the extension to a dynamical spacetime).

Besides this small difference, the merger takes places at almost the same time as for model 1.62-45-IF, namely, after about 2.5 orbits, or equivalently after 5.8 ms from the beginning of the simulation. However, the post-merger evolution of the HMNS is considerably different. This is nicely summarized in Fig. 12, which reports the evolution of the maximum rest-mass density normalized to its initial value and which, after the AH is found, refers to the region outside the AH. In this case shocks are allowed to form and the HMNS *does not* collapse promptly to a BH but, rather, undergoes very large oscillations with variations of 100% in the maximum of the rest-mass density (cf. Fig. 12). These oscillations are the result of what appears to be a dynamical bar-mode instability which develops and is suppressed at least four times during the post-merger phase. More specifically, after the first initial merger at $t \sim 5$ ms, the two stellar cores break up again to produce a bar-deformed structure, which rotates for more than a period before disappearing as the cores merge again. This process takes place four times and the merged object becomes increasingly more compact as it loses angular momentum and thus spins progressively faster. This behavior is clearly imprinted in the gravitational-wave signal as we will illustrate in Sec. IV B.

Together with these large variations, the rest-mass density also experiences a secular growth similar to the one already discussed for the low-mass polytropic binary and, as discussed before, the increased compactness eventually leads, at $t \sim 14$ ms, to the collapse to a rotating BH. The use of the isolated-horizon formalism reveals that in this case the final BH has a mass $M_{\rm BH} = 2.94 M_\odot$, spin $J_{\rm BH} = 7.3 M_\odot^2 = 6.4 \times 10^{49}$ g cm^2 s^{-1}, and thus a dimensionless spin $a \equiv J_{\rm BH}/M_{\rm BH}^2 = 0.85$ (cf. Table II).

The explanation for this behavior in the post-merger phase and the appearance, also at high masses, of a *delayed* collapse to BH, can be found by considering the component of the specific internal energy which is produced by the shock heating. This can be done by splitting the specific internal energy ϵ into a cold component $\epsilon_{\rm cold} = K\rho^{\Gamma-1}/(\Gamma-1)$ and into a thermal one $\epsilon_{\rm th}$, defined as [111]

$$\epsilon_{\rm th} = \epsilon - \epsilon_{\rm cold} = \frac{p}{\rho(\Gamma-1)} - \frac{K\rho^{\Gamma-1}}{\Gamma-1}. \qquad (25)$$

[Note that Eq. (13) of Ref. [111] contains a typo for the expression of $\epsilon_{\rm cold}$, which is corrected in expression (25)]. Figure 13 then reports the evolution of the coordinate volume-integral of the thermal part of the internal energy density $\int_V \rho \epsilon_{\rm th} dx^3$, which increases secularly soon after the merger (vertical dotted line) [indicated with the shaded area is the window in time in which the calculation of $\epsilon_{\rm th}$ via Eq. (25) becomes inaccurate as a result of the steep gradients in the hydrodynamical variables developing inside the AH]. We recall that in the case of an isentropic EOS (such as the polytropic EOS), $\epsilon_{\rm th} = 0$ and the quantity $\epsilon/\rho^{\Gamma-1}$ is constant and proportional to the specific entropy of the system. However, with a nonisentropic EOS (such as the ideal-fluid EOS), entropy increases across shocks and the latter are clearly present during the merger, thus leading to a local and global increase of the specific internal energy, namely, of $\epsilon_{\rm th}$. As a result, soon after the merger (vertical dotted line in Fig. 13), the HMNS from an ideal-fluid high-mass binary can rely on an additional pressure support, which allows it to balance the gravitational forces at least for a few additional ms. Stated differently, the shocks produced at the merger are responsible for a local and global increase of the temperature, which will produce a global expansion of the HMNS and thus a reduction of its compactness. The overall smaller compactness caused by the increased internal energy can be appreciated by comparing the fourth and fifth panels of Figs. 1 and 12.

A simple estimate for the temperature increase can be made by using the thermal part of the specific internal energy $\epsilon_{\rm th}$ and by neglecting the thermal energy due to radiation, so that $\epsilon_{\rm th} = 3kT/(2m_n)$, where k is the Boltzmann constant and m_n the rest mass of a nucleon.

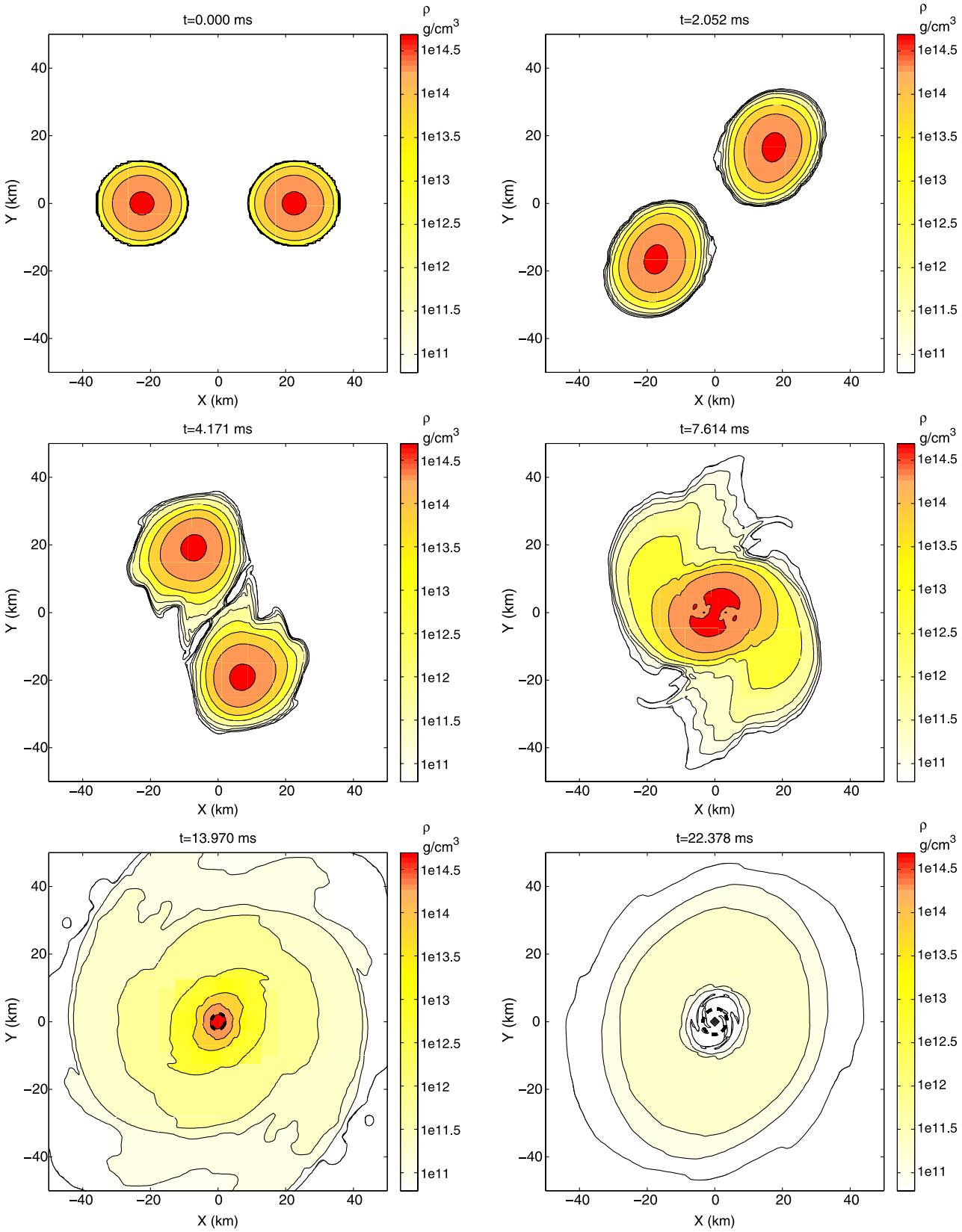

FIG. 11 (color online). Isodensity contours on the (x, y) (equatorial) plane for the evolution of the high-mass binary with the ideal-fluid EOS (i.e. model 1.62-45-IF in Table I). The time stamp in ms is shown on the top of each panel, the color-coding bar is shown on the right in units of g/cm^3, and the thick dashed line represents the AH.

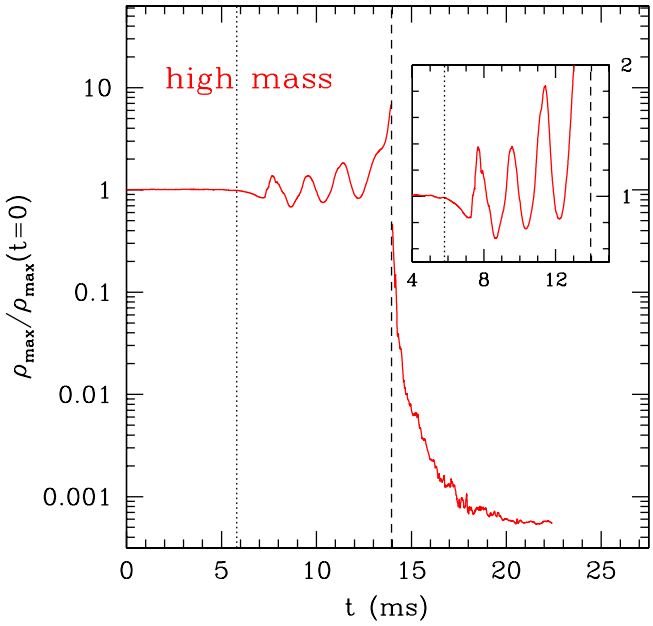

FIG. 12 (color online). Evolution of the maximum rest-mass density normalized to its initial value for the high-mass binary using the ideal-fluid EOS. Indicated with a dotted vertical line is the time at which the binary merges, while a vertical dashed line shows the time at which an AH is found. After this time, the maximum rest-mass density is computed in a region outside the AH. This figure should be compared with Fig. 2.

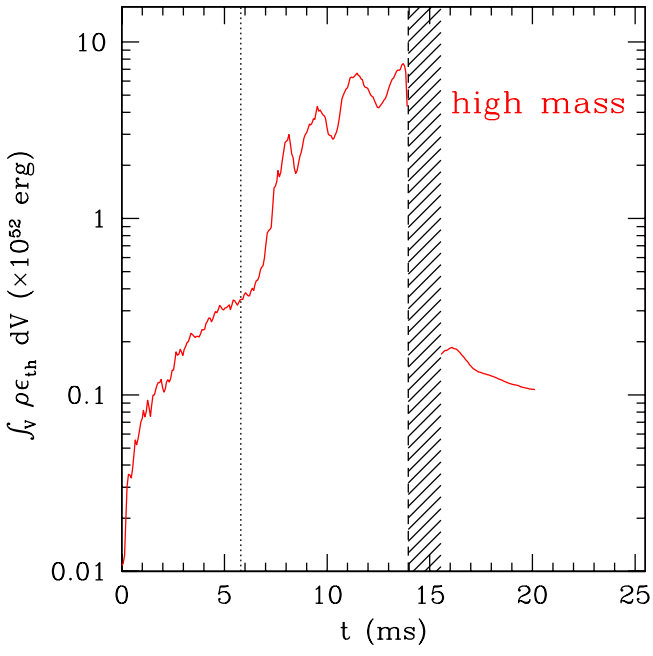

FIG. 13 (color online). Evolution of the coordinate volume-integral of the thermal part of the internal energy density. Note the secular increase in the thermal energy after the merger (vertical dotted line). The shaded area refers to a window in time in which the calculation of ϵ_{th} via Eq. (25) becomes inaccurate as a result of the steep gradients in the hydrodynamical variables developing inside the AH.

In this way the temperature is simply expressed as

$$T = \frac{2m_n}{3k(\Gamma-1)}\left[\frac{p}{\rho} - K\rho^{\Gamma-1}\right] \simeq \frac{7.2174\times 10^{12}}{\Gamma-1}\left[\frac{p}{\rho} - K\rho^{\Gamma-1}\right] \mathrm{K}. \quad (26)$$

Using (26) it is then possible to estimate that the HMNS has an initial temperature of 5×10^{10} K, which rapidly increases to 5×10^{11} K as the stellar cores merge. The additional shocks produced by the large oscillations in the post-merger phase can increase locally the temperature above these values, with maximum values that can reach 2×10^{12} K. Clearly, at such large temperatures the radiative losses, either via photons or neutrinos, can become very important and lead to a qualitative change from the evolution described here. While first attempts of introducing the contribution of radiative losses in general-relativistic calculations have recently been made (see, e.g. Refs. [112,113]), we are still far from a mathematically consistent and physically accurate treatment of these processes, which we will include in future works. For the time being it is sufficient to underline that, while it is clear that the inclusion of radiative processes will lead, quite generically, to a decrease in the survival time of the HMNS after the merger, determining this time with any reasonable precision will require not only the inclusion of radiative transport but also of a more realistic treatment of the EOS and of the scattering properties of the matter in the HMNS.

In the absence of a more detailed calculation of the radiative losses, we can here resort to simpler back-of-the-envelope calculations to assess the importance of radiative cooling in the post-merger phase when taking into account neutrino emission and diffusion. Let us therefore assume that the newly produced HMNS from a high-mass binary is approximately spherical with an average radius of $R_{\rm HMNS}\sim 20$ km, a mass of $M_{\rm HMNS}\sim 3.2M_\odot$, and thus an average rest-mass density which is essentially the nuclear rest-mass density, i.e. $\rho_{\rm HMNS}\sim\rho_{\rm nuc}\sim 3\times 10^{14}$ g/cm^3. We can now consider two different cooling processes acting either via modified-URCA emission (see Chap. 11 of Ref. [114]) or through the more efficient direct-URCA emission [115]. Assuming an initial average temperature of $T_{\rm HMNS}\sim 10^{11}$ K, the HMNS would cool down via modified-URCA processes to $T_{\rm HMNS}\sim 10^{10}(10^9)$ K in about 20 s (1 yr). On the other hand, if the cooling takes place through the much more efficient direct-URCA processes, the cooling time would be $\sim$3 ms (1 min). Because the latter interval is smaller or comparable with the $\sim$9 ms elapsing in the present calculations between the formation of the HMNS and its collapse to a BH, we conclude that radiative losses in the HMNS would accelerate its collapse to a BH only if direct-URCA processes take place.

Quite predictably, also the merger of a high-mass binary evolved with the ideal-fluid EOS leads to the formation of a torus orbiting around the BH. With respect to the high-

mass polytropic binary, however, the torus here has a different shape and a considerably larger vertical extension. Indeed the ratio of the vertical and horizontal sizes is ~ 0.5, while this was ~ 0.1 in the case of a polytropic EOS, irrespective of the mass of the binary. Consequently, the measured initial rest mass of the torus is of a factor 6 larger than the one of the corresponding high-mass polytropic binary, namely $(M_{\rm T})_{3\ {\rm ms}} = 0.0726 M_\odot$ instead of $(M_{\rm T})_{3\ {\rm ms}} = 0.0117 M_\odot$, 3 ms after the first measure (cf. Table II). The average density, on the other hand, is considerably smaller (between 10^{11} and 10^{12} g/cm^3).

The dynamics of the torus are summarized in Fig. 14, which shows the isodensity contours on the (x, z) plane; note again that the panels refer to times between 14.0 ms and 22.4 ms and thus to a stage in the evolution which is between the last two panels of Fig. 14. A simple comparison between Figs. 3, 10, and 14 is sufficient to capture the differences among the tori in the three different cases considered so far.

In view of the discussion made above on the increased internal energy content produced by the shocks in the case of the ideal-fluid EOS, the formation of a vertically extended torus is not at all surprising, but the obvious response of the matter of the torus to a larger (thermal) pressure gradient in the vertical direction. Interestingly, the maximum rest-mass density of the torus does not show the typical harmonic behavior discussed so far in the case of the polytropic binaries and produced by the quasiperiodic oscillations in the radial direction. Rather, the maximum density shows a clear and monotonic decrease with time as a result of the accretion of the torus onto the BH (cf. Fig. 12 for $t \gtrsim 14$ ms). At the same time, the maximum of the internal energy in the torus is seen to increase (cf. Fig. 13 for $t \gtrsim 14$ ms). Both the higher temperature and the geometrically thick shape of the torus produced in this case provide an important evidence that the merger of a massive NS binary could lead to the physical conditions behind the generation of a GRB. A more detailed analysis of the energetics and properties of the torus (and, in particular, of its variability in time) is needed to further support this possibility and it will be presented in a future work [90].

D. Ideal-fluid EOS: low-mass binary

Despite it being significantly different from the evolution of both the low-mass polytropic binary and of the high-mass ideal-fluid binary, the dynamics of the low-mass ideal-fluid binary is rather simple. In particular, the two NSs merge at essentially the same time as the corresponding high-mass ideal-fluid binary (i.e. $t \simeq 5.8$ ms) and produce a HMNS which is, however, not sufficiently massive to collapse promptly to a BH. Rather, the HMNS undergoes a bar-mode instability producing an $m = 2$

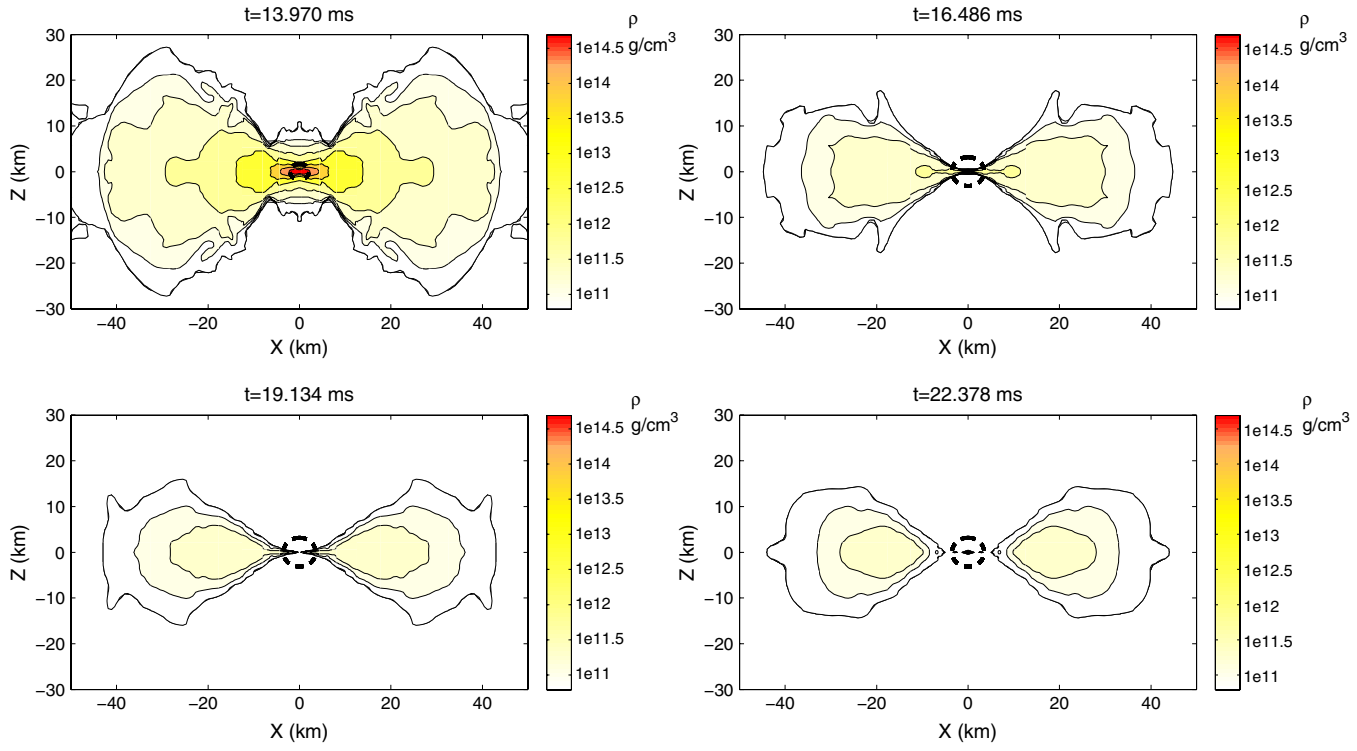

FIG. 14 (color online). Isodensity contours on the (x, z) plane highlighting the formation of a torus surrounding the central BH, whose AH is indicated with a thick dashed line. The data refer to the high-mass binary evolved with the ideal-fluid EOS (cf. Figs. 3 and 10 and the different vertical scales.)

deformation as the system tries to reach a configuration which is energetically favorable.

Either as a result of the π-symmetry imposed (and which prevents the growth of the $m = 1$ mode) or simply because the HMNS is very close to the threshold of the bar-mode instability, the bar is seen to persist for the whole time the calculations were carried out, i.e. $\sim$30 ms (see the discussion of Ref. [13] about under what conditions a bar-mode deformation is expected to survive over a longer time scale; recent additional work on this can also be found in Ref. [116]). Note that the bar deformation remains only approximately constant in time and that small oscillations in the central rest-mass density can be measured. This is shown in Fig. 15, which reports the evolution of the maximum rest-mass density normalized to its initial value. Indicated with a dotted vertical line is the time at which the stars merge. This figure should be compared with Figs. 2, 8, and 12, of which it maintains the same scale.

During this rather long period of time (corresponding to $\sim$16 revolutions) the HMNS also loses large amounts of angular momentum through gravitational radiation (see discussion in Secs. IV B and IV C). As a result, the compactness of the HMNS gradually increases and the central density shows the characteristic secular increase already discussed for the previous binaries (cf. inset of Fig. 15). The radiation-reaction time scale is in this case much longer: the HMNS is not very massive (its mass of $\approx 2.6 M_\odot$ is only $\approx 10\%$ larger than the supramassive

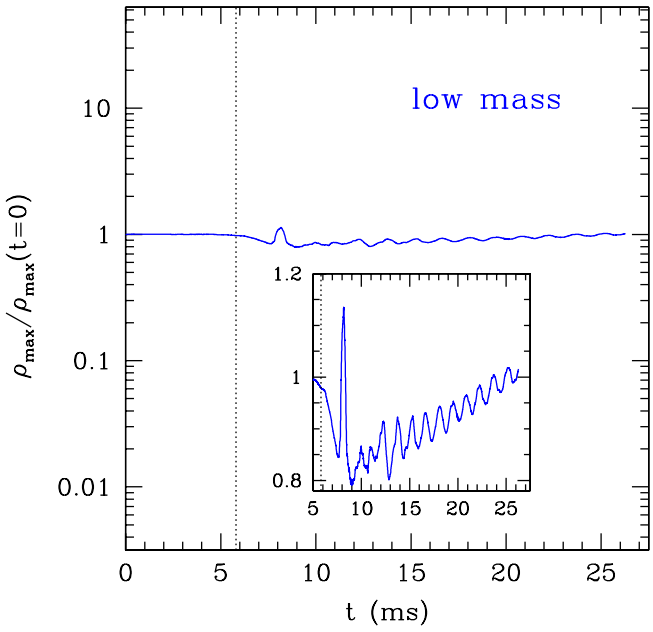

FIG. 15 (color online). Evolution of the maximum rest-mass density normalized to its initial value for the low-mass binary evolved using the ideal-fluid EOS. Indicated with a dotted vertical line is the time at which the binary merges. This figure should be compared with Figs. 2, 8, and 12, of which maintains the same scale.

limit) and is more extended as a result of the increased internal temperature. As a result, the migration to the unstable branch and the collapse to a BH will occur much later than what was calculated and shown in Fig. 15. Using the latter to compute the growth rate of the maximum rest-mass density and assuming that the collapse to a BH is triggered when $\rho_{max}/\rho_{max}(t = 0) \simeq 2$ (cf. Figs. 2 and 12), we estimate that the collapse will take place at $t \sim 110$ ms. This time scale should be compared with the corresponding one (i.e. $\sim$21 ms) obtained from the same initial data but evolved with a polytropic EOS. Clearly, the increase in the internal energy via shocks is responsible for this "long delay" in the collapse to a BH.

As a final comment we note that a time scale of $\sim$110 ms is much longer than what is computationally feasible at the moment. As a result, the analysis of this binary will be limited to a time interval of $\sim$30 ms, which is, however, long enough to deduce its most interesting properties (see discussion in Secs. IV B and IV C).

E. Vortex sheet and Kelvin-Helmholtz instability

As mentioned above, when the two stars come into contact a vortex sheet (or shear interface) develops there where the tangential components of the velocity exhibit a discontinuity (i.e. the x and y components of the three-velocity in our setup). This condition is known to be unstable to very small perturbations and it can develop a Kelvin-Helmholtz instability, which will curl the interface forming a series of vortices [117]. This is indeed what we observe in all our simulations, with features that are essentially not dependent on the mass or on the EOS used.

In the left panel of Fig. 16 we show the isodensity contours and the velocity vector field on the equatorial plane for the high-mass binary evolved with a polytropic EOS at a time $t = 6.091$ ms when the presence of vortices is particularly evident. The density is shown in units of g/cm^3 and in the bottom-right part of the plot an arrow is used as a reference for the values of the velocity. Furthermore, in order to highlight the formation of the shear interface, we have removed from the total velocity field the orbital angular velocity defined as the angular velocity of the stellar centers. The vector-field representation shows rather clearly that the vortex sheet goes from the bottom-left corner of the plot to the upper-right one. Along this sheet one can observe at least four main vortices, two of which are located at [$x \approx \pm 7$ km, $y \approx \pm 5$ km], while the other two are smaller and located at [$x \approx 0$ km, $y \approx \pm 2$ km]. It is worth remarking that, because these smaller vortices have a scale of $\gtrsim 2$ km $\sim 1.3 M_\odot$, they are well captured by our resolution in the central regions which, we recall, is $h = 0.12 M_\odot \approx 0.177$ km. Because the employed numerical methods are very weakly dissipative on these scales, we believe that our description of the Kelvin-Helmholtz instability is indeed accurate at the scales presented. Of course, different resolutions will either remove

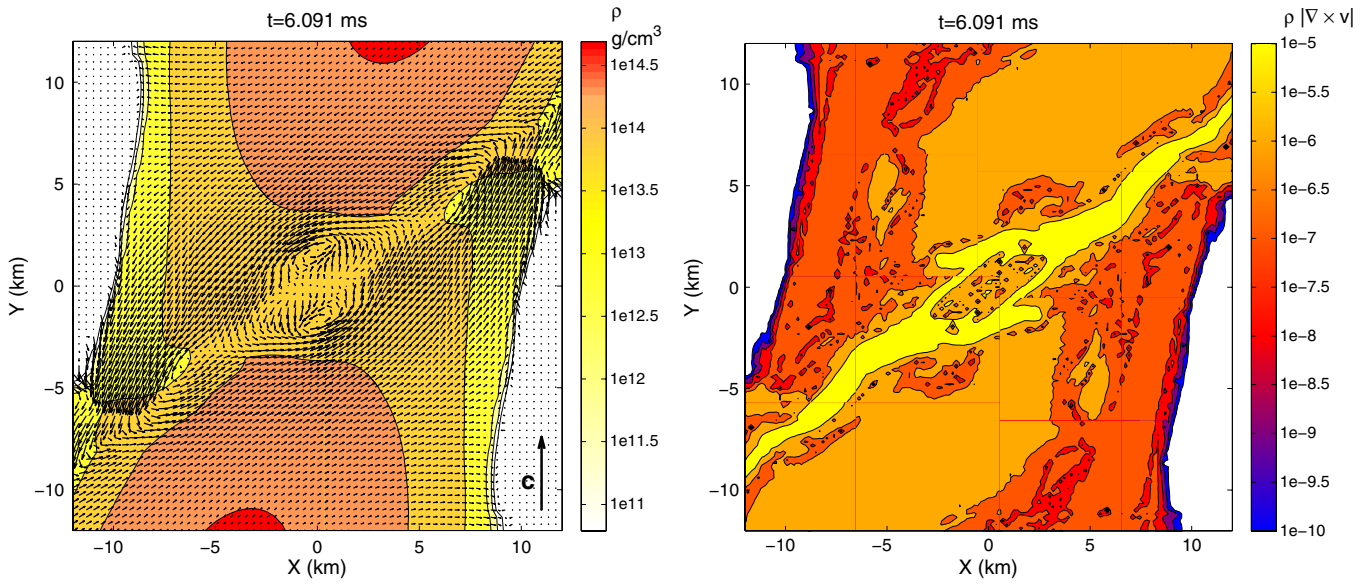

FIG. 16 (color online). *Left panel:* Isodensity contours and velocity vector field (with the orbital component removed) on the (x, y) (equatorial) plane at a selected time soon after the merger. Note the presence of localized vortices in the shear layer between the two stars. *Right panel:* contours of the weighted vorticity $\rho|\nabla \times \mathbf{v}|^z$ (that is the rest-mass density multiplied by the module of the z component of the vorticity) for the same time shown in the left panel. This rendering highlights that in the shear layer the vorticity can be up to 3 orders of magnitude larger than in the bulk of the stars. Both panels refer to a high-mass binary evolved with the polytropic EOS.

some of the vortices (as the resolution is decreased) or introduce new ones (as the resolution is increased). In practice, we have found that a vortex of scale λ is lost when the resolution used is $h \gtrsim 0.2\lambda$, probably because the intrinsic numerical dissipation prevents their formation.

A different and novel way of showing the presence of a vortex sheet and of the consequent development of a Kelvin-Helmholtz instability is offered in the right panel of Fig. 16, which shows the contours of the "weighted vorticity" on the equatorial plane, i.e. $\rho|\nabla \times \mathbf{v}|^z$. Although this vector represents the Newtonian limit of the general-relativistic vorticity tensor $\omega_{\mu\nu} = \partial_{[\nu}(hu_{\mu])}$ [118], it serves the purpose here of being proportional to the latter and also of simpler calculation. Because the color coding is made in a logarithmic scale, the right panel of Fig. 16 clearly highlights that the vorticity is not uniform in the merged object but that its value in the vortex sheet is up to three orders of magnitude larger than in the bulk of the stars. As stressed above, while both panels of Fig. 16 refer to the high-mass polytropic binary, very similar results were obtained also for the low-mass binary or with the ideal-fluid EOS.

To quantify the development of the Kelvin-Helmholtz instability and measure its growth rate we have computed the maximum of the weighted vorticity in the equatorial plane and plotted its time evolution in Fig. 17, where it is also shown as divided by the maximum of the rest-mass density to remove the contribution due to the increase in ρ after the merger. Shown with different lines are the weighted vorticities for the high-mass binary (solid line) and for the low-mass binary (dashed line), evolved either with a polytropic EOS (left panel) or with an ideal-fluid EOS (right panel). Also indicated with a vertical dotted line is the time at which the two NSs merge, while the two vertical dashed lines refer to the times at which the AH is found in the two cases (no evolution is shown past this time as the measure of the vorticity becomes much more complex because of the turbulent motions in the torus). It is evident that after an initial growth of a factor of a few between $t = 0$ and $t = 2$ ms, probably produced by the transient away from the initial data, the weighted vorticity remains approximately small and constant. This stops at the time of the merger at $t \approx 5$ ms (cf. dotted vertical line) when the weighted vorticity grows exponentially of about 2 orders of magnitude. The Newtonian perturbative expectation for the growth rate is $\sigma \sim \pi v/\lambda$ where v is the value of the velocity at the shear interface and λ is the wavelength of the smallest growing mode; for $v \sim 10^{-2}$ and $\lambda \sim 2$ km, the measured growth rate is $\sigma \simeq 10^3$ s^{-1} and in reasonable agreement with the Newtonian expectation.

The instability rapidly saturates when the two stellar cores merge; as a result, after $\sim$2 ms from its initial development it reaches a quasistationary state. Note that the growth rate is essentially the same for the high- and low-mass binary and for the two EOSs (cf. the two panels Fig. 17); however, the evolution after the saturation is different for the different masses. The high-mass binaries

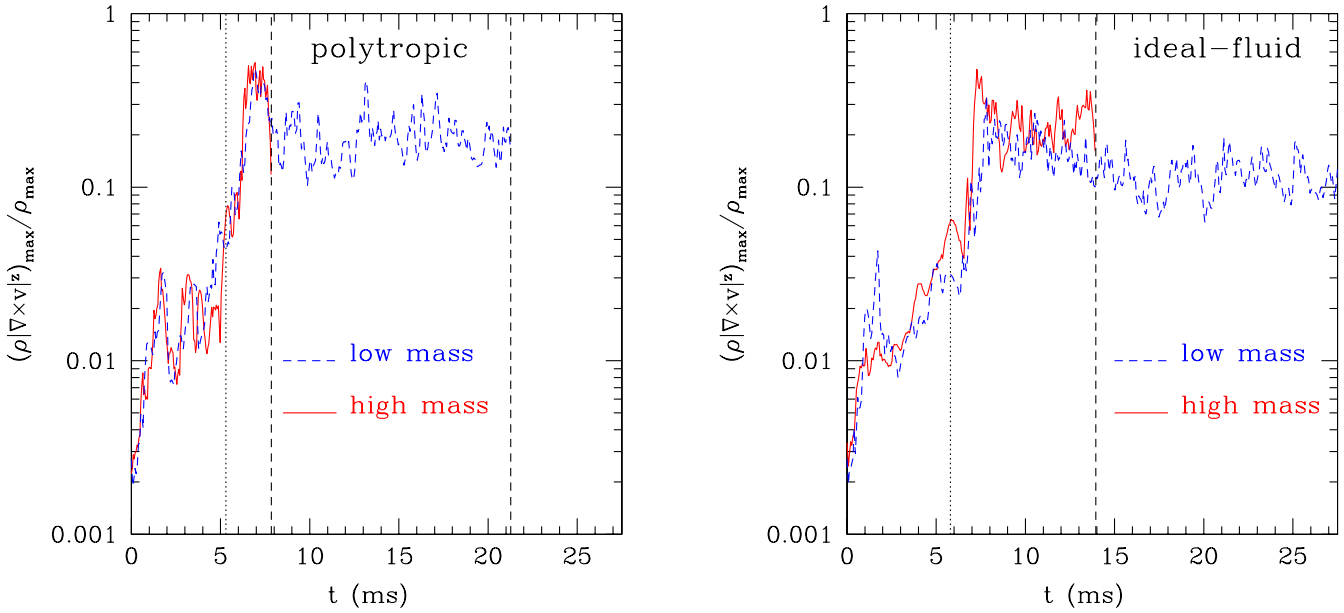

FIG. 17 (color online). *Left panel:* Maximum of the weighted vorticity $\rho|\nabla \times \mathbf{v}|^z$ on the equatorial plane normalized by the maximum of the rest-mass density $\rho_{\max}$ during the evolution of the high (solid line) and low (dashed line) mass binaries evolved with the polytropic EOS. Indicated with a dotted vertical line is the time at which the binaries merge. Both the curves are plotted until the formation of an AH. *Right panel:* The same as in the left panel but for the ideal-fluid EOS.

collapse to a BH, while the HMNSs produced by the low-mass binaries hang on for a longer time, during which the instability persists at almost constant amplitude [for $\sim$13 ms (cf. dashed line in Fig. 17)].

As a final remark we note that, even if this instability is purely hydrodynamical, it can have strong consequences when studying the dynamics of binary NSs in the presence of magnetic fields. Indeed, as first shown by [48] in Newtonian simulations and later briefly reported also by [49] in general-relativistic calculations, in the presence of a magnetic field this instability leads to an exponential growth of the toroidal component even if the initial magnetic field is a purely poloidal one. In particular, it is reasonable to expect that even a moderate initial poloidal magnetic field of $\approx 10^{12}$ G can be increased up to values of order 10^{15} G through this mechanism. Such high values of the magnetic fields are the ones presumed to be behind the phenomenology in magnetars, but are also thought to be the values necessary in order to extract sufficient energy from a system composed by a torus orbiting around a BH and power short hard GRBs. Work is now in progress for the investigation of this mechanism in fully general-relativistic MHD using the code presented in [51]; results of this investigation will soon be reported in a distinct article.

IV. GRAVITATIONAL-WAVE EMISSION

The accurate determination of the gravitational-radiation content of the simulated spacetimes represents a delicate and yet fundamental aspect of any modeling of sources of gravitational waves; in view of this, we have implemented two different and equivalent methods to compute the gravitational waves produced by the binary evolution. The possibility of a comparison between the two methods and the cross-validation of the results provides us with additional confidence that the extracted waveforms are not only numerically accurate but also physically consistent.

The first method uses the Newman-Penrose formalism, which provides a convenient representation for a number of radiation-related quantities as spin-weighted scalars. In particular, the curvature scalar

$$\Psi_4 \equiv -C_{\alpha\beta\gamma\delta} n^\alpha \bar{m}^\beta n^\gamma \bar{m}^\delta \tag{27}$$

is defined as a particular component of the Weyl curvature tensor, $C_{\alpha\beta\gamma\delta}$, projected onto a given null frame $\{\boldsymbol{l}, \mathbf{n}, \mathbf{m}, \bar{\mathbf{m}}\}$ and can be identified with the gravitational radiation if a suitable frame is chosen at the extraction radius. In practice, we define an orthonormal basis in the three space $(\hat{\mathbf{r}}, \hat{\boldsymbol{\theta}}, \hat{\boldsymbol{\phi}})$, centered on the Cartesian origin and oriented with poles along $\hat{\mathbf{z}}$. The normal to the slice defines a timelike vector $\hat{\mathbf{t}}$, from which we construct the null frame

$$\boldsymbol{l} = \tfrac{1}{\sqrt{2}}(\hat{\mathbf{t}} - \hat{\mathbf{r}}), \qquad \mathbf{n} = \tfrac{1}{\sqrt{2}}(\hat{\mathbf{t}} + \hat{\mathbf{r}}), \qquad \mathbf{m} = \tfrac{1}{\sqrt{2}}(\hat{\boldsymbol{\theta}} - \mathrm{i}\hat{\boldsymbol{\phi}}). \tag{28}$$

We then calculate Ψ_4 via a reformulation of (27) in terms of ADM variables on the slice [119],

$$\Psi_4 = C_{ij} \bar{m}^i \bar{m}^j, \tag{29}$$

where

$$C_{ij} \equiv R_{ij} - KK_{ij} + K_i^k K_{kj} - \mathrm{i}\epsilon_i^{kl}\nabla_l K_{jk}. \quad (30)$$

The gravitational-wave polarization amplitudes h_+ and $h_\times$ are then related to Ψ_4 by simple time integrals [120]

$$\ddot{h}_+ - \mathrm{i}\ddot{h}_\times = \Psi_4, \quad (31)$$

where the double overdot stands for the second-order time derivative.

The second and independent method is instead based on the measurements of the nonspherical gauge-invariant perturbations of a Schwarzschild BH (see Refs. [121–123] for some applications of this method to Cartesian-coordinate grids). In practice, a set of "observers" is placed on 2-spheres of fixed Schwarzschild radius r_S, derived from the coordinate (isotropic) radius via the standard formula

$$r_S = r_{iso}\left(1 - \frac{M}{2r_{iso}}\right)^2, \quad (32)$$

where $M = M_{ADM}$ is assumed constant throughout the simulation. On these 2-spheres we extract the gauge-invariant, odd-parity (or *axial*) current multipoles $Q^\times_{\ell m}$ and even-parity (or *polar*) mass multipoles $Q^+_{\ell m}$ of the metric perturbation [124,125]. The $Q^+_{\ell m}$ and $Q^\times_{\ell m}$ variables are related to h_+ and $h_\times$ as [126]

$$h_+ - \mathrm{i}h_\times = \frac{1}{\sqrt{2}r}\sum_{\ell,m}\left(Q^+_{\ell m} - \mathrm{i}\int_{-\infty}^{t} Q^\times_{\ell m}(t')dt'\right){}_{-2}Y^{\ell m}. \quad (33)$$

Here ${}_{-2}Y^{\ell m}$ are the $s = -2$ spin-weighted spherical harmonics and (ℓ, m) are the indices of the angular decomposition.

A. Waveforms from polytropic binaries

In what follows we illustrate and discuss the gravitational-wave signal produced by the inspiral and merger of the binaries discussed in Sec. III and we start by discussing the waveforms produced by the binaries evolved with the polytropic EOS.

Figure 18, in particular, shows in the left panel the retarded-time evolution of the real part of the $\ell = m = 2$ component of $r\Psi_4$ as extracted from a 2-sphere at a coordinate radius $r = 200M_\odot = 295$ km for the high-mass binary. Hereafter $r = 200M_\odot = 295$ km will be the extraction radius for all the waveforms presented, unless specified differently. Indicated in the inset is the final part of the signal corresponding to the BH quasinormal ringing. We recall that the merger takes place at $(t - r) \sim 5.3$ ms and that an AH is first found at $(t - r) = 7.85$ ms. The gravitational-wave signal during the inspiral is clearly very well captured and remarkably reminiscent of the one observed in the many binary BH simulations performed to date (see, for instance, [127,128] and references therein) and deviations from this type of waveforms are evident

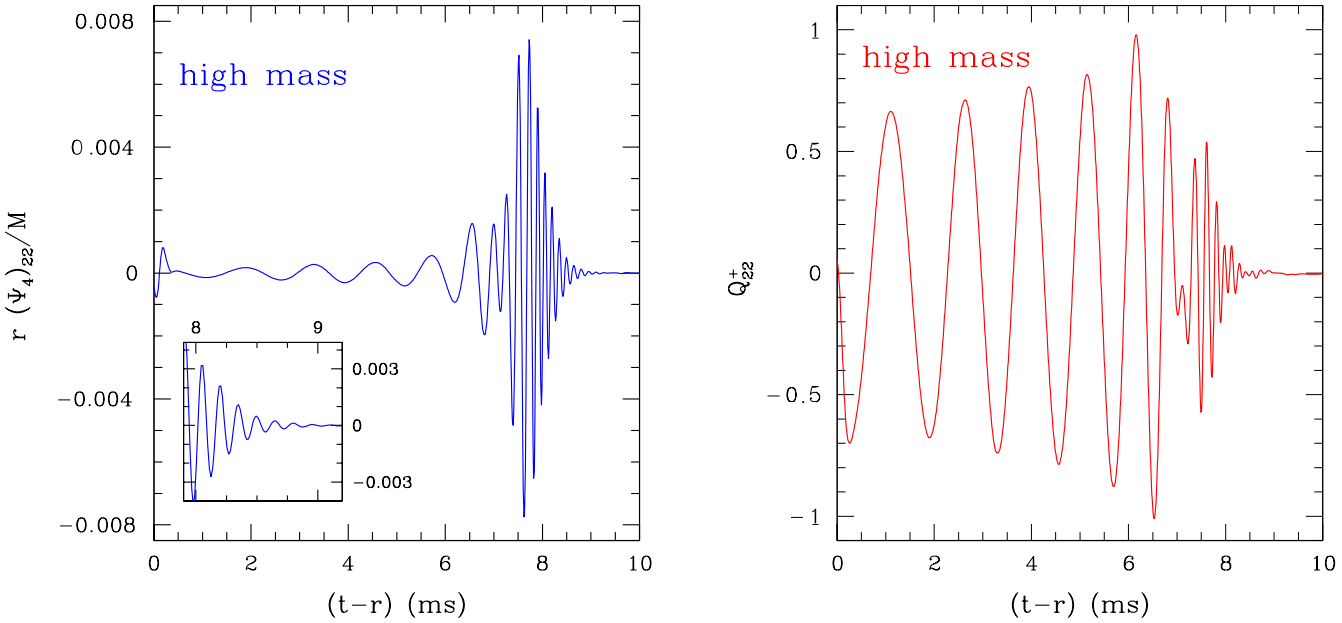

FIG. 18 (color online). *Left panel*: Retarded-time evolution of the real part of the $\ell = m = 2$ component of $r\Psi_4$ as extracted from a 2-sphere at a coordinate radius $r = 200M_\odot = 295$ km for the high-mass binary. Indicated in the inset is the final part of the signal corresponding to the BH quasinormal ringing. The merger takes place at $(t - r) \sim 5.3$ ms. *Right panel*: The same as in the left panel but shown in terms of the real part of the gauge-invariant quantity Q^+_{22}. In both cases the binaries have been evolved using the polytropic EOS.

only at $(t - r) \simeq 7$ ms, when the HMNS starts its collapse to a BH. The ability of reproducing accurately the exponential decay of the quasinormal ringing is often a good indication of having reached a sufficient level of accuracy as this involves the ability of measuring changes in the fields on the smallest possible physical scales (i.e. that of the horizon). The clean quasinormal ringing shown in the inset shows that this is indeed the case for the simulations reported here.

It should also be added that, because the newly formed BH is not in vacuum but rather surrounded by a relativistic and accreting torus, the gravitational-wave signal should not be expected to be exponentially decaying to infinitesimal amplitudes during the ringdown. This explains the tiny but nonzero oscillations which can be seen after the ringdown and which are probably related to the accretion of matter onto the BH. A comparison with the results of Refs. [95,96,99] or with the perturbative analysis of Ref. [129] could help to clarify the properties of this signal.

The right panel of Fig. 18, on the other hand, shows the gravitational-wave signal in terms of the real part of the gauge-invariant quantity Q_{22}^{+}. Because in this case the odd perturbations have zero real and imaginary part, the time evolution of the real (imaginary) part of Q_{22}^{+} corresponds, modulo a constant coefficient, to the time evolution of the $\ell = m = 2$ component of $h_{+}(h_{\times})$. Note that the two waveforms are clearly different, but this is simply because they differ by two time derivatives [cf. Eqs. (31) and (33)]. In fact, if a double time integral is made of the Ψ_4-waveforms, the corresponding curve lies on top of the one for Q_{22}^{+}, after a suitable normalization (see also Fig. 14 of Ref. [67] where this was shown in the case of binary black holes).

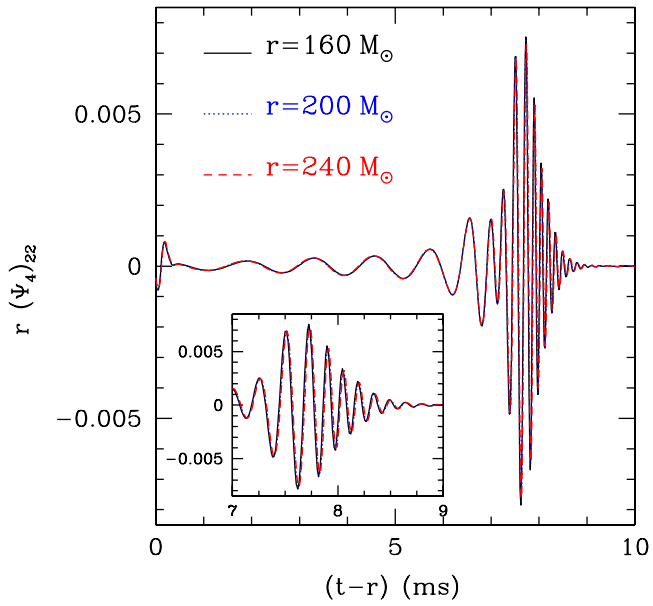

FIG. 19 (color online). Comparison of the real part of the $\ell = m = 2$ component of $r\Psi_4$ for the high-mass binary evolved with the polytropic EOS when extracted at different radii: $r = 160M_{\odot} = 236$ km (solid line), $r = 200M_{\odot} = 295$ km (dashed line), and $r = 240M_{\odot} = 354$ km (dotted line).

The comparison offered by Fig. 18 is useful to illustrate that, in contrast with what happens for binary BHs, the amplitude of the h_{+} and $h_{\times}$ polarizations does not increase monotonically in time but, rather, is reduced as the two NSs merge and as the HMNS collapses to a BH. Nevertheless, as we will comment in Sec. IV C, the energy loss rate is largest during these stages (cf. right panel of Fig. 24).

Another important validation that the signal extracted corresponds to gravitational radiation can be obtained by verifying that Ψ_4 satisfies the expected "peeling" properties of the Weyl scalars, i.e. $r^{5-n}\Psi_n = \text{const}$. This is illustrated in Fig. 19 which compares the real part of the $\ell = m = 2$ component of Ψ_4 when extracted at three considerably different radii: $r = 160M_{\odot} = 236$ km (solid line), $r = 200M_{\odot} = 295$ km (dotted line), and $r = 240M_{\odot} = 354$ km (dashed line) (the last radius is close to the outer boundary of our computational domain). Clearly, the overlap among the different waveforms is very good both in phase and in amplitude and indicates that already at $r \sim 150M_{\odot} = 222$ km gravitational waves can be extracted with confidence. (A similar figure can be built using the Schwarzschild perturbations and has not been shown here for compactness).

It is interesting now to reconsider the impact that different initial separations of the same binary have on the emitted gravitational-wave signal. This aspect was already discussed in Sec. III A, where the different dynamics were considered, and nicely summarized in Figs. 4 and 6. We recall that the conclusions reached in Sec. III A were that the differences in the evolution of the large-separation binary 1.62-60-P and of its corresponding small-separation equivalent 1.62-45-P had to be found mostly in the internal structure and thus they were absent in the premerger evolution of both the central rest-mass density (cf. Fig. 6) and the proper separation. A similar conclusion can be drawn also for the waveforms and we show in Fig. 20 a comparison in the real part of the $\ell = m = 2$ component of Ψ_4 (upper panel) for the high-mass binaries evolved starting from an initial separation of 45 or 60 km. Note that the waveform for the 1.62-60-P binary contains more than 10 gravitational-wave cycles and is, therefore, the longest general-relativistic waveform computed to date.

An equivalent view of this comparison is shown in the lower panel of Fig. 20 which reports instead the amplitude of Ψ_4. Indicated with dashed lines in both panels are the values after a suitable time shift. The good overlap in the inspiral phase is what is expected on PN grounds; however, a closer inspection also reveals that small differences do appear and these can then be used as a measure of the high-order PN corrections coming from compact binaries with finite size. More work and the use of long waveforms are necessary to study this further.

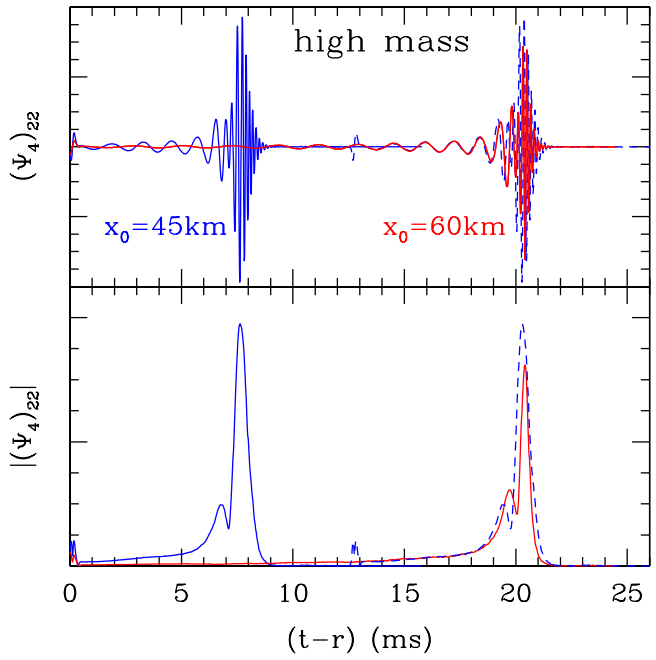

FIG. 20 (color online). Comparison of the real part of the $\ell = m = 2$ component of $r\Psi_4$ (upper panel) and of its amplitude (lower panel) for the high-mass binaries evolved with the polytropic EOS starting from an initial separation of 45 or 60 km. Indicated with a dashed line are the values after a time-shift.

We conclude this section by discussing the gravitational-wave signal emitted by the low-mass binary and reported in Fig. 21. Also in this case we show in the left panel the retarded-time evolution of the real part of the $\ell = m = 2$ component of $r\Psi_4$, while in the right panel the real part of the gauge-invariant quantity Q^+_{22}. As mentioned in the previous section, the HMNS has a prominent $m = 2$ bar deformation and gradually evolves towards a configuration which is unstable to gravitational collapse through the emission of gravitational waves. The loss of energy and angular momentum progressively reduces the centrifugal support and increases the compactness of the HMNS which, as a result, spins more rapidly. This is particularly clear in the evolution of Ψ_4, which is shown in the left panel of Fig. 21 and which exhibits the typical increase in amplitude and frequency of the gravitational-wave signal. This runaway behavior ends at the time of the formation of the BH, which then rings down exponentially as shown in the two insets. A rapid comparison of Figs. 18 and 21 is sufficient to appreciate the marked differences introduced in the evolution of the binary by a different initial mass. In the following section this comparison will be carried out also across different EOSs (cf. Fig. 23).

B. Waveforms from ideal-fluid binaries

As mentioned when discussing the dynamics of ideal-fluid binaries, the significant differences that emerged both for the evolution of high- and low-mass binaries are reflected in their gravitational-wave emission. We recall that ideal-fluid binaries will experience a considerable increase of their internal energy (temperature) as a result of the shocks produced at the merger. As a result, a high-mass binary exhibits a delay in the collapse to BH of ~8 ms,

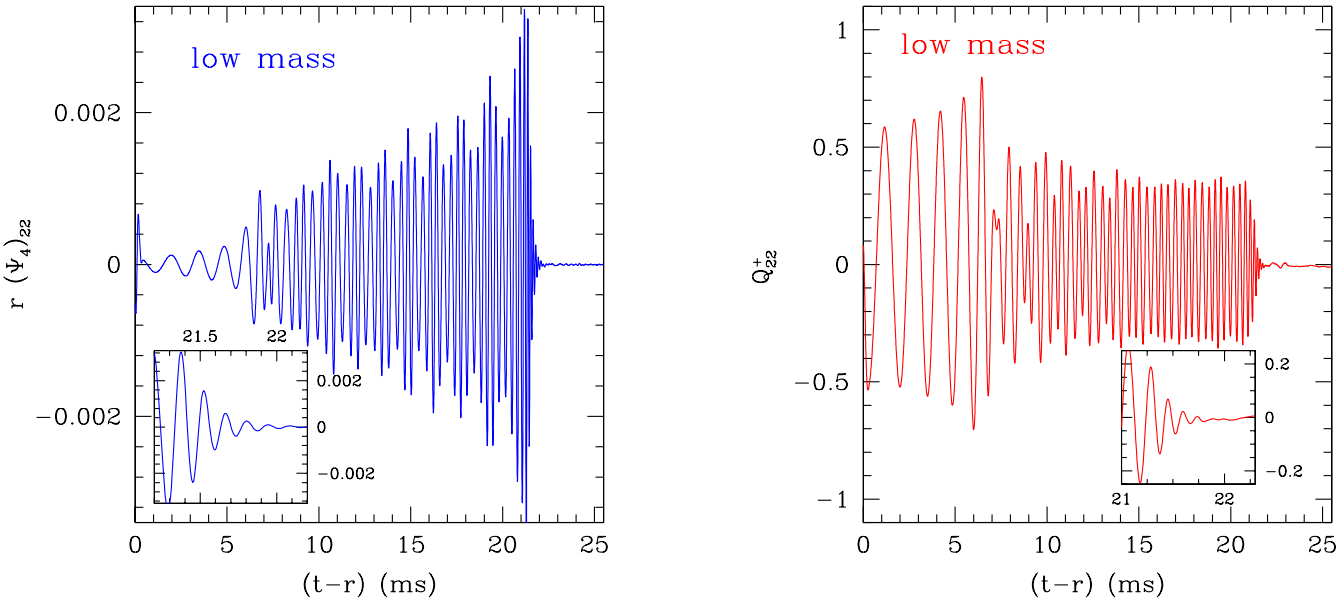

FIG. 21 (color online). *Left panel*: Retarded-time evolution of the real part of the $\ell = m = 2$ component of $r\Psi_4$ for the low-mass binary. Indicated in the inset is the final part of the signal corresponding to the BH quasinormal ringing. The merger takes place at $(t - r) \sim 5.3$ ms. *Right panel*: The same as in the left panel but shown in terms of the real part of the gauge-invariant quantity Q^+_{22}. In both cases the binaries have been evolved using the *polytropic* EOS.

which should be contrasted with the corresponding ~3 ms obtained for the same binary when evolved with a polytropic EOS. Similarly, a low-mass binary will show a much longer delay, which we estimated to be ~105 ms and which is to be contrasted with the corresponding ~16 ms obtained for the same binary when evolved with a polytropic EOS.

This is nicely summarized in Fig. 22, whose left panel shows the retarded-time evolution of the real part of the $\ell = m = 2$ component of $r\Psi_4$ for the high-mass binary. As commented in Sec. III C, the HMNS undergoes repeatedly a dynamical bar-mode instability which develops and is suppressed at least four times during the post-merger phase, as the two stellar cores merge. The HMNS becomes increasingly more compact as it loses angular momentum and thus spins progressively faster. This behavior is clearly imprinted in the gravitational-wave signal and it is easy to distinguish the four stages of the bar development at times $t \sim 8$, 10, 12, and 14 ms, respectively. The last one is accompanied also by the gravitational collapse to BH and exhibits a well-captured quasinormal ringing.

The right panel of Fig. 22, on the other hand, refers to the low-mass binary and has a straightforward interpretation: the HMNS produced has a small $m = 2$ deformation and is still too far from the instability threshold to the collapse to a BH. Rather, the bar rapidly reaches an equilibrium configuration which persists over the 16 revolutions over which the calculations were carried out. The resulting waveforms are produced at twice the frequency of the revolution of the bar, i.e. at ~2 kHz, and show a remarkably constant amplitude (cf. inset in the right panel of Fig. 22). It is still unclear whether the stability of the deformation is the result of the bar being very close to the dynamical instability threshold or the result of the imposed π-symmetry, which prevents the growth and coupling of the $m = 1$ and $m = 2$ modes [13,116]. Clarifying this point will require calculations which are at least twice as expensive but it will be essential to determine whether the corresponding gravitational-wave spectrum will be characterized by a large and predominant peak at ~2 kHz (cf. right panel of Fig. 27).

Figure 23 offers in its left panel a comparison in retarded-time evolution of the real part of the $\ell = m = 2$ component of $r\Psi_4$ for the high-mass binaries when evolved with the polytropic or with the ideal-fluid EOS (cf. left panels of Figs. 18 and 22). When shown in the same graph, it becomes much easier to appreciate the impact that the nonisentropic nature of the ideal-fluid EOS has on the dynamics of the merger and, most importantly, on the gravitational-wave emission. Clearly, when the waveforms from merging binary NSs will be detected, they will effectively provide the Rosetta stone for the deciphering of the stellar structure and EOS. In addition, the comparison in Fig. 23 can also be used to gauge the possible range of behaviors that a more realistic treatment of the matter may yield. Both a polytropic and an ideal-fluid EOS, in fact, can be considered as the extremes of such a behavior, with either a perfectly adiabatic evolution in which shocks (and hence shock heating) cannot occur, or with an evolution in which local increases of the tempera-

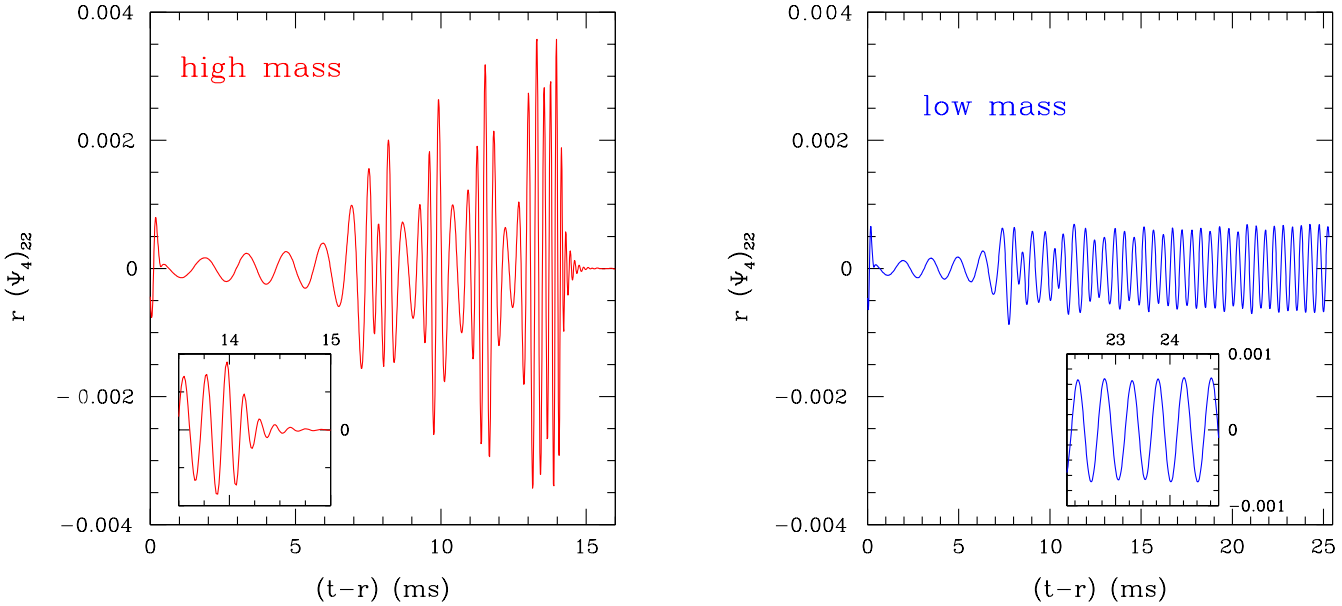

FIG. 22 (color online). *Left panel:* Retarded-time evolution of the real part of the $\ell = m = 2$ component of $r\Psi_4$ for the high-mass binary evolved with the ideal-fluid EOS. Indicated in the inset is the final part of the signal corresponding to the BH quasinormal ringing. *Right panel:* The same as in the left panel but for the low-mass binary. Here the inset does not refer to the BH quasinormal ringing; it highlights, instead, the periodic nature of the gravitational radiation after the merger. In both cases the merger takes place at $(t - r) \sim 5.8$ ms.

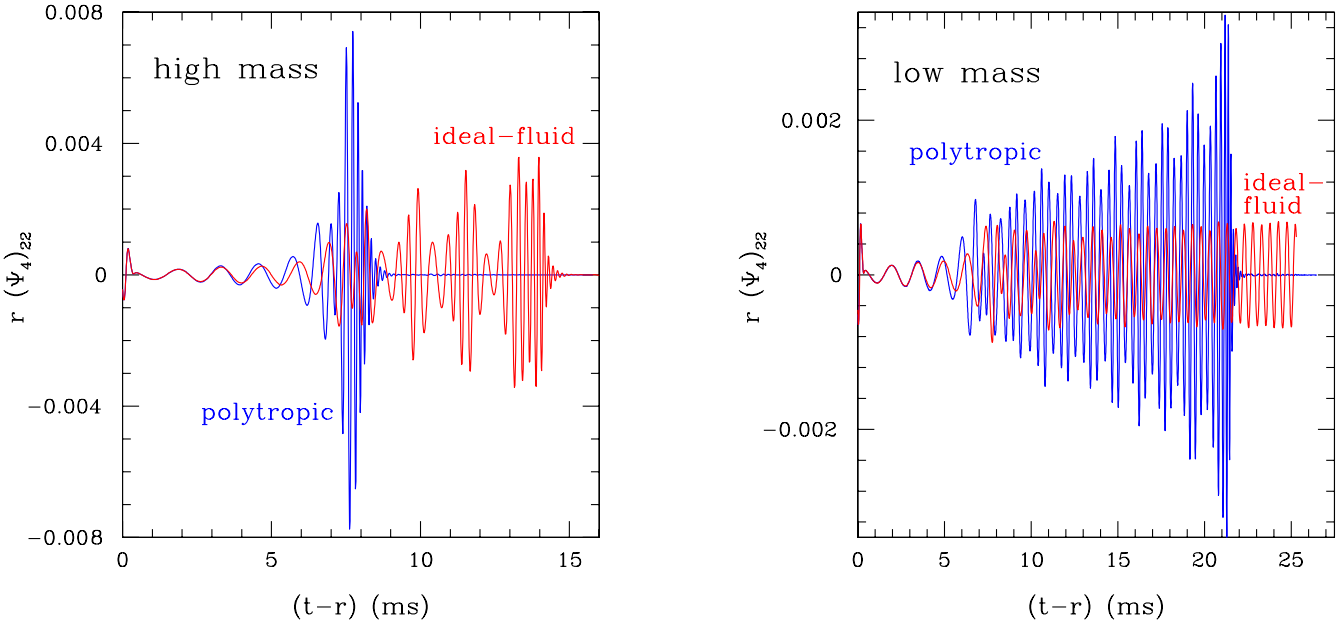

FIG. 23 (color online). *Left panel:* Comparison in retarded-time evolution of the real part of the $\ell = m = 2$ component of $r\Psi_4$ for the high-mass binary when evolved with the polytropic or with the ideal-fluid EOS. *Right panel:* The same as in the left panel but for the low-mass binary.

ture through shocks are allowed but cannot lead to radiative processes. Furthermore, because neutrinos or photons are expected to be trapped and would be able to leave the system only on diffusion time scales, any realistic EOS will lead to evolutions similar to those observed with the nonisentropic ideal-fluid EOS.

Finally, the right panel of Fig. 23 is the same as in the left panel but for the low-mass binaries (cf. left panel of Figs. 21 and right panel of Fig. 22). Also in this case the analogies and differences have a straightforward interpretation and underline the importance of considering the time between the merger and the collapse to BH as an important indicator of the properties of the binary.

C. Energy and angular-momentum losses

We have computed the energy and the angular momentum carried away by gravitational waves using the even and odd-parity perturbations, $Q^{+}_{\ell m}$ and $Q^{\times}_{\ell m}$, respectively. The rate of energy loss, simply given by [126]

$$\frac{dE_{\rm GW}}{dt} = \frac{1}{32\pi}\sum_{\ell,m}\left(\left|\frac{dQ^{+}_{\ell m}}{dt}\right|^2 + |Q^{\times}_{\ell m}|^2\right), \qquad (34)$$

is shown in the right panel of Fig. 24 for all the low-mass and high-mass binaries considered here. In the left panel of the same figure we show the value of $E_{\rm GW}$ normalized to the initial ADM mass of the system $M_{\rm ADM}$ as a function of the retarded time $t - r$ where $r = 200M_\odot = 295$ km is the radius at which the waveforms were extracted. In both panels the solid line refers to the high-mass polytropic model 1.62-45-P, the dashed line to the high-mass ideal-fluid case 1.62-45-IF, the dotted line to the low-mass polytropic binary 1.46-45-P, the dotted-dashed line to the low-mass ideal-fluid one 1.46-45-IF, and finally the long-dashed line to the high-mass polytropic model with an initial separation of 60 km, namely, 1.62-60-P.

From the right panel of Fig. 24 it is evident that all the models have a first maximum in the energy emission rate soon after the merger. This initial increase in the emission rate is related to the last part of the inspiral phase, when the amplitude and the frequency of the gravitational-wave signal increase. After this first peak, however, the emission rate has a substantial drop, which is common to all the models and it is due to a very short (i.e. $\ll 1$ ms) transition phase in which the deviations from axisymmetric are smaller. We now concentrate on describing the different dynamics of the different models after this initial common part, i.e. on the emission rate related to the evolution of the system after the merger.

In the case of the two high-mass polytropic binaries, i.e. 1.62-45-P and 1.62-60-P, there is also a second peak in the energy emission at the time of the collapse and, except for the different times at which the merger and the subsequent collapse to BH take place, their profiles are very similar, with a total energy emitted which is $\sim 0.01 M_{\rm ADM}$. This second peak, which has an amplitude comparable to or higher than the first one, is simply related to the increase in amplitude and frequency of the gravitational waves emitted during the collapse (see also Fig. 20). In the case of the high-mass binary evolved with an ideal-fluid EOS, however, the emission rate exhibits four peaks after the merger and this is due to the different post-merger dynamics. As

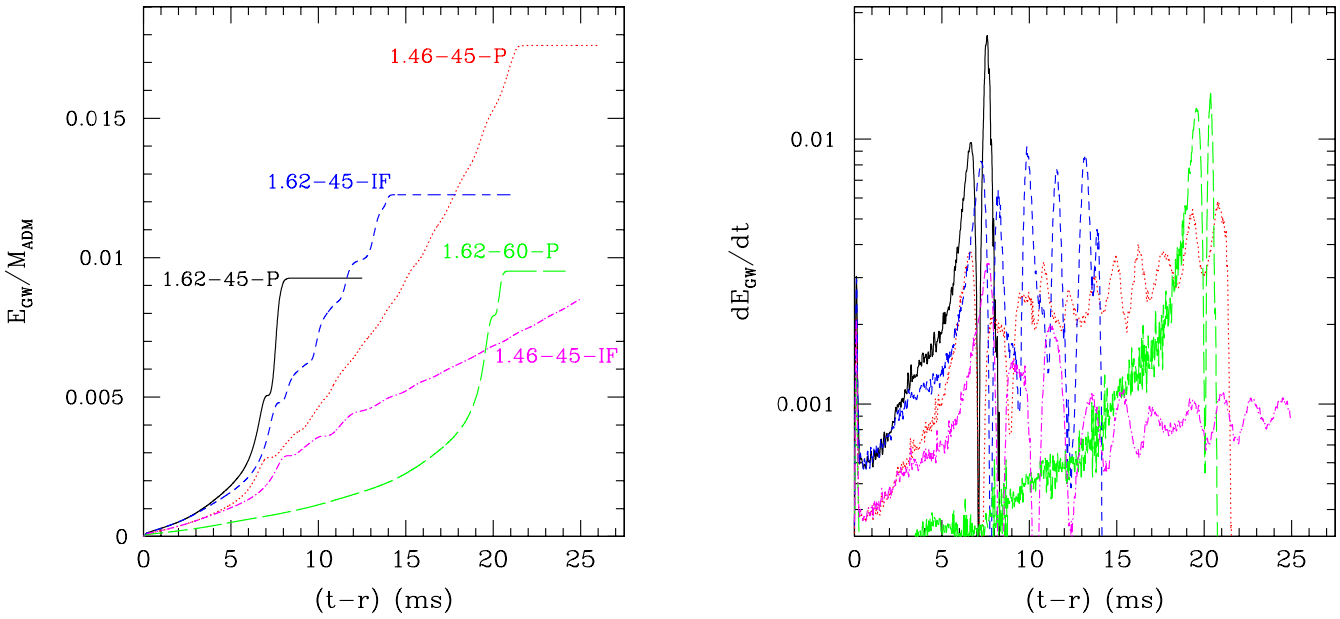

FIG. 24 (color online). *Left panel*: Energy emitted in gravitational waves for the high-mass binary evolved with a polytropic EOS (solid line), for the low-mass binary evolved with a polytropic EOS (dotted line), for the high-mass binary evolved with the ideal-fluid EOS (dashed line), and for the low-mass binary evolved with the ideal-fluid EOS (dot-dashed line). Note that the largest amount of radiation comes from the low-mass binary whose emission has not been computed before. Indicated with a long-dashed line is the high-mass polytropic binary starting at 60 km. *Right panel*: The same as in the left panel but for the rate of the energy loss. Note that the largest burst of radiation is produced by the high-mass polytropic binary at the time of the prompt collapse to a BH.

already discussed in Sec. III C, instead of collapsing promptly to a BH as the polytropic one, this system forms a bar-shaped HMNS with the high-density cores of the two NSs periodically merging and bouncing until sufficient angular momentum is carried away and the collapse starts. These periodic bounces and mergers of the two cores determine the several peaks seen in the emission rates. At the end, the total energy radiated through gravitational-waves is larger than the one emitted in the polytropic case and is $\simeq 0.012 M_{\rm ADM}$.

For the two low-mass binaries, 1.46-45-P and 1.46-45-IF, on the other hand, the emission rate is always smaller than for the high-mass binaries, but it shows several peaks and for a longer time. This is related to the dynamics of the bar-deformed HMNSs that rotate for several stellar periods before collapsing to BHs. As a result, even if the emission rate is smaller, the total energy emitted in gravitational waves is much larger and in the case of the low-mass polytropic binary is $\simeq 0.018 M_{\rm ADM}$ at the time of the collapse, while for the low-mass ideal-fluid binary it can be estimated to be $\approx 0.04 M_{\rm ADM}$ when extrapolating the time of the collapse to $t \approx 110$ ms (see discussion in Sec. III D).

The two panels in Fig. 24 are particularly useful to appreciate and quantify the differences that emerge among different binaries in the inspiral phase and, later on, in the post-merger phase. It is particularly instructive to consider the similarity in the evolutions of binaries having the same initial separation and mass, but different EOS, i.e. 1.62-45-P and 1.62-45-IF or 1.46-45-P and 1.46-45-IF. We recall that these sets of binaries have exactly the same initial data and hence the differences during the inspiral are due uniquely to the role played by the EOS. As clearly shown in the left panel of Fig. 24, these differences are very small, so that 1.62-45-P and 1.62-45-IF have lost to gravitational waves essentially the same amount of mass at the time of the merger, although the latter actually takes place at slightly different times (i.e. $t \sim 5.3$ ms for 1.62-45-P and $t \sim 5.8$ ms for 1.62-45-IF; see the discussion in Sec. III C). Because an identical comment also applies for 1.46-45-P and 1.46-45-IF, we conclude that the EOS introduces major differences in the binary evolutions only *after* the merger.

On the contrary, for binaries having the same EOS but different masses (e.g. binaries 1.62-45-P and 1.46-45-P), also the evolution *before* the merger is different and can contribute to different post-merger evolutions (see the comment below on the angular-momentum losses).

In a similar way, we have computed the angular-momentum loss as [126]

$$\frac{dJ_{\rm GW}(t)}{dt} = \frac{1}{32\pi}\sum_{\ell,m} im\left[\frac{dQ^{+}_{\ell m}}{dt}(Q^{+}_{\ell m})^{*} + Q^{\times}_{\ell m}\int_{-\infty}^{t}(Q^{\times}_{\ell m})^{*}(t')dt'\right] \qquad (35)$$

and, in analogy with Fig. 24, of which we use the same line-type convention, we show in the left panel of Fig. 25 the loss of angular momentum normalized to the initial

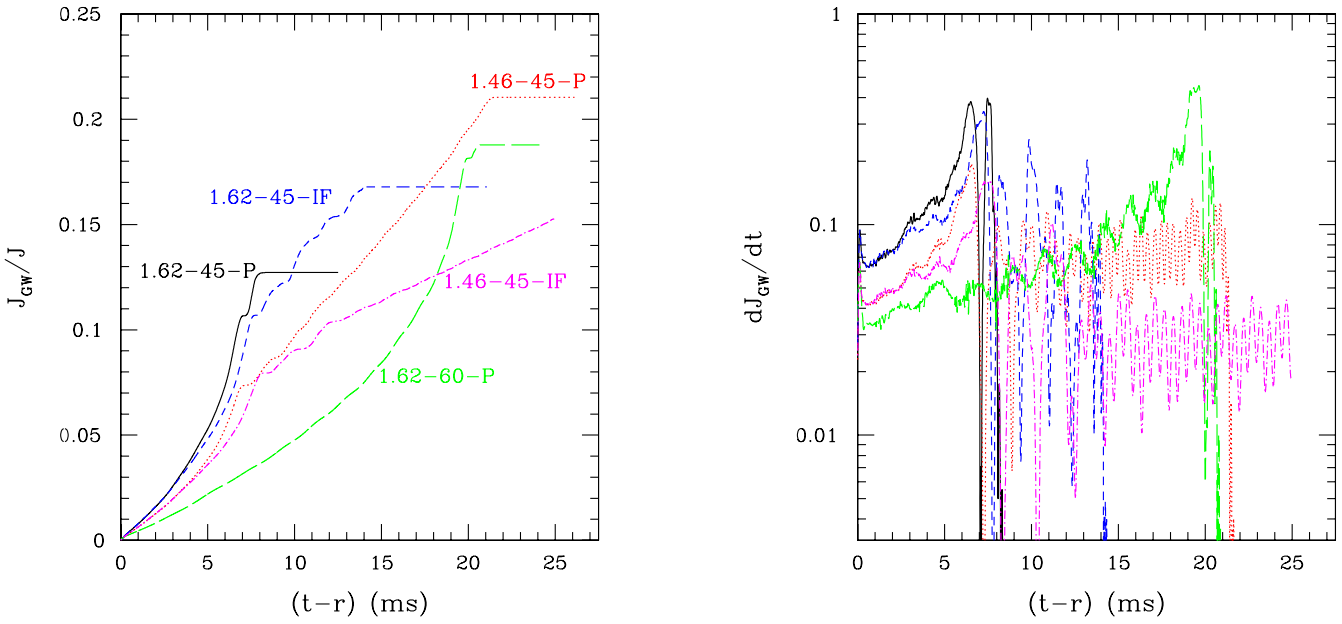

FIG. 25 (color online). *Left panel*: The same as in Fig. 24 but for the orbital angular momentum normalized to its initial value (cf. Table I). *Right panel*: The same as in Fig. 24 but for the rate of loss of orbital angular momentum.

angular momentum of the system and in the right panel the loss rate.

Overall, the angular-momentum losses and loss rates follow rather closely the behavior already discussed for the energy, namely, there is very little difference during the inspiral for binaries having the same mass. When looking more carefully, however, it is possible to note that the evolution of the angular momentum shows small differences after about 3 ms even for binaries with the same mass, e.g. 1.62-45-P and 1.62-45-IF. This time corresponds roughly to that of the first orbit, after which the nonisentropic evolution of model 1.62-45-IF will have changed the stellar structure only slightly but in a manner sufficient to produce a different emission of gravitational waves and hence a different loss of angular momentum. Indeed it is clear from the left panel of Fig. 25 that the merger begins when the two binaries have lost $\sim$1% of their initial angular momentum but that this takes place at different times for the two binaries, happening earlier for model 1.62-45-P which is isentropic, more compact, and with a larger quadrupole moment.

More marked are the differences seen when comparing binaries differing only in the mass (e.g. binaries 1.62-45-P and 1.46-45-P or binaries 1.62-45-IF and 1.46-45-IF). We recall that these two sets of binaries essentially merge at the same time and it is then apparent from Fig. 25 that at the time of the merger the high-mass binary will have lost a larger relative amount of the initial orbital angular momentum. As a result, the matter orbiting outside the AH when this forms will also have a smaller amount of angular momentum and is therefore more likely to be more rapidly accreted. This explains why the high-mass polytropic binary 1.62-45-P produces a torus with a smaller rest mass than the low-mass polytropic binary 1.46-45-P, both at the AH formation and after 3 ms (cf. Table II).[6]

This behavior indicates that, at least for binaries having the same EOS, the rate of loss of angular momentum during the inspiral phase plays an important role in determining the final mass of the torus and that the models that lose less angular momentum during the inspiral, hence comparatively *low-mass* binaries, are expected to have comparatively *high-mass* tori. This confirms what is already observed in Ref. [44].

Note, however, that such a simple conclusion is strictly true for binaries having the same EOS and when no radiative losses are taken into account. Under more generic conditions, however, the EOS is also expected to play an important role and a representative example comes from comparing the high-mass binaries 1.62-45-P and 1.62-45-IF. In this case, in fact, the loss of angular momentum during the inspiral is essentially the same (cf. left panel of Fig. 25), but it is substantially different after the merger, with a loss of angular momentum which is at least 50% larger for the ideal-fluid binary. Yet, because of the increased pressure support the latter produces a torus with a mass which is $\sim$7 times larger than the corresponding one for the polytropic binary.

[6]Since we cannot follow the low-mass ideal-fluid binary till BH formation we cannot verify that this conclusion holds also for the ideal-fluid binaries, although we expect so.

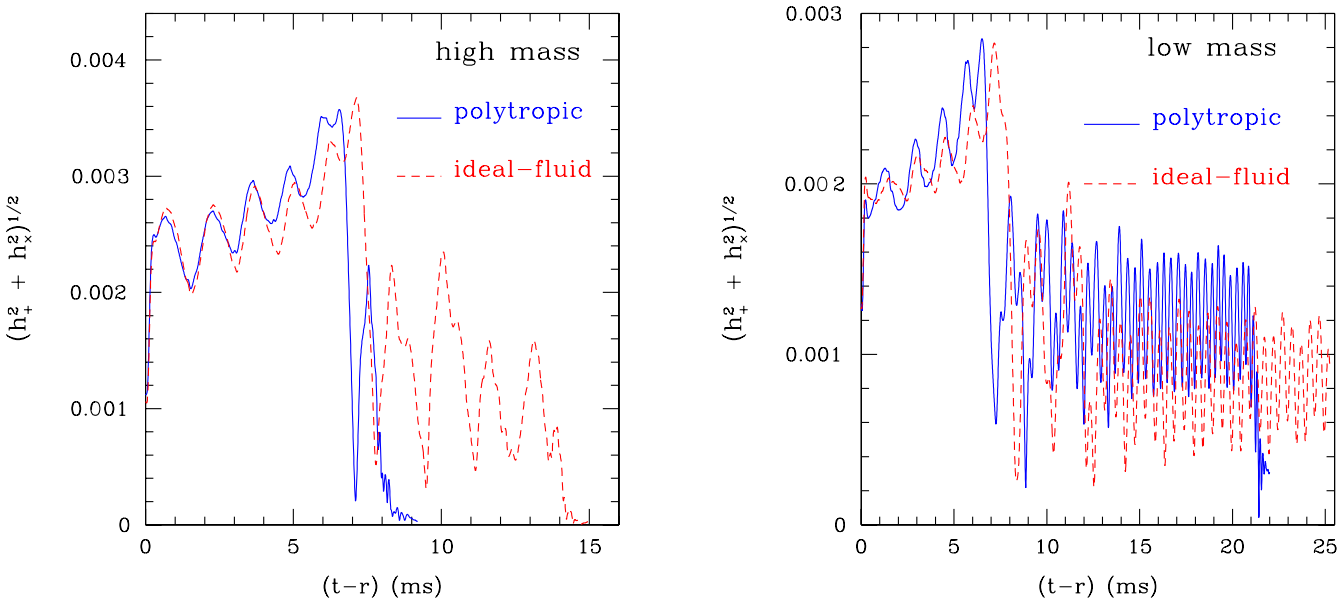

FIG. 26 (color online). *Left panel*: Comparison of retarded-time evolution of the amplitude the $\ell = m = 2$ component of $h = (h_+^2 + h_\times^2)$ for the high-mass binary when evolved with the polytropic (solid line) or with the ideal-fluid (dashed line) EOS; cf., Fig. 23, left panel. *Right panel*: The same as in the left panel but for the low-mass binary; cf., Fig. 23, right panel.

D. Gravitational-wave spectra and signal-to-noise ratios

We have also studied and compared the amplitudes and frequencies of the gravitational-wave signal produced by the different models. In particular in Fig. 26 we plot the amplitude of the $\ell = m = 2$ component of the total gravitational-wave amplitude $\sqrt{h_+^2(t) + h_\times^2(t)}$ [where we neglect the contribution of the spin-weighted spherical harmonic $-2Y^{22}$ in Eq. (33)], for four different binaries, all starting from an initial separation of 45 km, as a function of the retarded time $t - r$, where $r = 200M_\odot = 295$ km is the radius at which the signal was extracted. In particular, in the right panel we show the evolution of the gravitational-wave amplitude for the low-mass binaries 1.46-45-* evolved using a polytropic EOS (solid line) and an ideal-fluid EOS (dashed line) while in the left panel we show the same but for the high-mass binaries 1.62-45-*. We recall that for all of these models the merger takes place after ≈ 5 ms, which corresponds to the time when the amplitude reaches its maximum. The slight difference in the position of these maxima between the polytropic and the ideal-fluid binaries is related to the difference in the time of the merger and is $\lesssim 1$ ms.

Since the dynamics in the inspiral are very similar, the two high-mass binaries have a very similar and increasing amplitude, up to the merger. Note, however, that the increase is not monotonic and this is due mostly to the presence of a nonzero eccentricity. As commented in Sec. III A, a good part of the eccentricity is due to gauge effects (and is significantly reduced when the shift vector is initially set to zero), but a small portion of it is also genuinely present in the initial data. Fortunately this spurious eccentricity has only a small impact in the power-spectral density (PSD) of the gravitational-wave signal and it is easy to isolate being it at ~ 4 times the orbital frequency. The evolution of the amplitude in the post-merger phase is rather different and, while it drops significantly for the polytropic binary, it remains at large values for the ideal-fluid binary as a result of the delayed collapse to the BH; as we will comment later on, this will have an impact also on the detectability of this signal.

The two low-mass binaries in the right panel of Fig. 26 also show a similar evolution up to the merger with an increase of the amplitude which is modulated by eccentricity and reaches its maximum at the merger. Of course, the maximum value reached in this case is lower than the one obtained in the high-mass cases. After the merger the amplitude is reduced by a factor of ~ 2 and remains to that level for the ≈ 15 ms which separate the merger and the collapse to a BH. In the case of the ideal-fluid binary, on the other hand, the post-merger amplitude is smaller and essentially constant for the whole time the simulation was carried out. As mentioned already, this binary is expected to collapse to a BH on a time scale of ~ 110 ms.

We next consider the gravitational-wave emission in the frequency domain and for this we have computed the power-spectral density of the effective amplitude

$$\tilde{h}(f) \equiv \sqrt{\frac{\tilde{h}_+^2(f) + \tilde{h}_\times^2(f)}{2}}, \tag{36}$$

where f is the gravitational-wave frequency and where

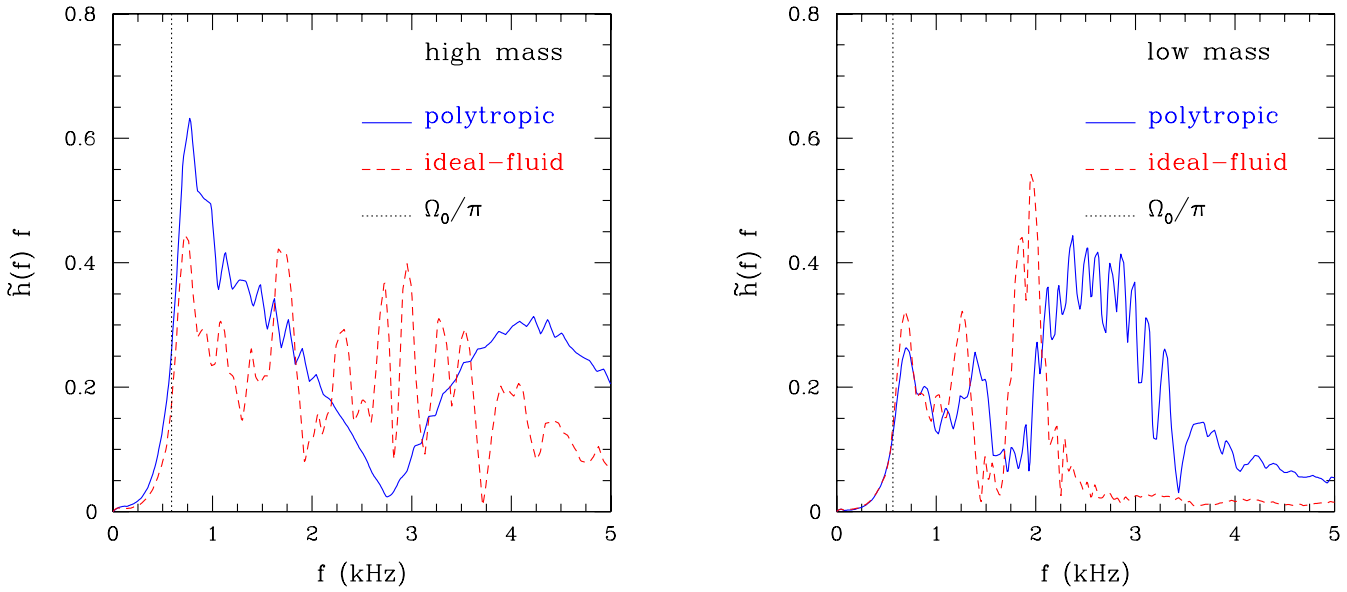

FIG. 27 (color online). *Left panel*: Comparison of the PSD of the $\ell = m = 2$ component of $h(f)f$ for the high-mass binary when evolved with the polytropic (solid line) or with the ideal-fluid (dashed line) EOS; cf., Fig. 23, left panel. *Right panel*: The same as in the left panel but for the low-mass binary; cf., Fig. 23, right panel. Indicated with a vertical long-dashed line is twice the initial orbital frequency.

$$\tilde{h}_{+,\times}(f) \equiv \int_0^\infty e^{2\pi i f t} h_{+,\times}(t) dt \tag{37}$$

are the Fourier transforms of the gravitational-wave amplitudes $h_{+,\times}(t)$, built using only the largest $\ell = m = 2$ multipole.

In Fig. 27 we compare the spectral distribution of the quantity $\tilde{h}(f)f$ for the high-mass binaries (left panel) and the low-mass binaries (right panel) when evolved with the two EOSs. In both cases we use a solid line for the polytropic binaries and a dashed line for the binaries evolved with the ideal-fluid EOS. Also indicated in both panels with a vertical long-dashed line is the frequency corresponding to twice the initial orbital frequency $f_0 \equiv \Omega_0/(2\pi)$ where $f_0 = 283$ Hz for the low-mass binaries and $f_0 = 295$ Hz for the high-mass ones. These frequencies are representative of the signal at the beginning of the simulated inspiral and thus represent lower cutoff frequencies, below which the PSD is not meaningful. On the other hand, the peaks in the PSDs observed at frequencies slightly larger than the orbital ones are very important as they refer to the power emitted during the inspiral.

The PSD for the high-mass polytropic binary (left panel of Fig. 27) is quite simple, as it shows, besides the inspiral peak, also a peak at $f \approx 4$ kHz, corresponding to the collapse of the HMNS (cf. left panel of Fig. 26). Note that the PSD shown does not include the frequency of the fundamental QNM of the newly produced BH. Using the approximate expression [130,131]

$$f_{\rm QNM} \approx 3.23 \left(\frac{M_{\rm BH}}{10 M_\odot}\right)^{-1} [1 - 0.63(1-a)^{0.3}]\ {\rm kHz}, \tag{38}$$

this frequency is $f_{\rm QNM} \simeq 6.7$ kHz for the BH produced by this binary (cf. Table III).

The PSD for the high-mass ideal-fluid binary, on the other hand, is more complex, with the inspiral peak at $f \approx 0.75$ kHz being accompanied by a number of other peaks,

TABLE III. Signal-to-noise ratio (SNR) computed for different detectors assuming a source at 10 Mpc. The different columns refer to: the proper separation between the centers of the stars $d/M_{\rm ADM}$; the baryon mass M_b of each star in solar masses; the total ADM mass $M_{\rm ADM}$ in solar masses, as measured on the finite-difference grid; the approximate quasinormal mode frequency of the fundamental mode $f_{\rm QNM}$ in kHz; the SNR for Virgo, LIGO, Advanced LIGO, and GEO.

Model	$d/M_{\rm ADM}$	$M_b(M_\odot)$	$M_{\rm ADM}(M_\odot)$	$f_{\rm QNM}$(kHz)	SNR (Virgo)	SNR (LIGO)	SNR (Adv. LIGO)	SNR (GEO)
1.46-45-P	14.3	1.456	2.681	7.3	1.92	1.33	12.54	0.57
1.46-45-IF	14.3	1.456	2.681	⋯	2.08	1.45	13.52	0.62
1.62-45-P	12.2	1.625	2.982	6.7	2.15	1.48	13.29	0.63
1.62-45-IF	12.2	1.625	2.982	7.0	2.29	1.57	14.42	0.67
1.62-60-P	16.8	1.625	2.987	6.5	3.97	3.15	35.52	1.48

the most prominent having a similar amplitude at $f \approx 1.75$ kHz and $f \approx 3$ kHz. These additional peaks (and also the smaller ones between the two) are obviously related to the post-merger phase at $t \gtrsim 5$ ms and, in particular, to the dynamics of the HMNS formed after the merger and especially to the dynamics of the cores of the two NSs, which merge and bounce several times before the HMNS collapses to a BH, producing a small peak at $f \approx 4$ kHz. Also in this case even the fundamental QNM has a frequency $f_{\rm QNM} \simeq 7.0$ kHz (cf. Table III) and is therefore outside the range shown in Fig. 27.

In a similar way it is possible to interpret the PSDs of the low-mass binaries. The polytropic one, in particular, shows an excess power at $f \approx 0.75$ kHz due to the inspiral but also a very broad peak between $f \approx 2$ kHz and $f \approx 3.5$ kHz, that is related to the dynamics of the bar-deformed HMNS formed after the merger and persisting for several milliseconds. Also in this case a small excess power is seen at $f \gtrsim 4$ kHz and is associated with the collapse to the BH, whose fundamental QNM has a frequency $f_{\rm QNM} \simeq 7.3$ kHz. Interestingly, the low-mass ideal-fluid PSD does not show the broad peak but a very narrow and high-amplitude one at $f \approx 2$ kHz. This is obviously related to the long-lived bar deformation of the HMNS, which we have followed for $\sim$16 revolutions (as computed from the cycles of the quadrupolar gravitational radiation). At this stage it is unclear whether this prominent peak will survive when the simulations are repeated without the use of a π-symmetry and more conclusive results on this will be presented elsewhere [90]. Note that the high-frequency part of the PSD for the low-mass ideal-fluid binary (i.e. for $f \gtrsim 2$ kHz) is essentially zero, because of the absence of a collapse to BH, which for this binary takes place in an excessively long time.

A fundamental piece of information necessary to assess the relevance of binary NSs as sources of gravitational waves comes from the calculation of the SNR which we have computed for interferometric detectors such as Virgo, LIGO, Advanced LIGO, and GEO. For all the models discussed above, including the high-mass polytropic binary with a larger initial separation of 60 km, the SNR has been computed as

$$\left(\frac{S}{N}\right)^2 = 4 \int_0^\infty \frac{|\tilde{h}_+(f)|^2}{S_h(f)} df, \tag{39}$$

where $S_h(f)$ is the noise power-spectral density for a given detector. The results computed assuming a source at a distance of 10 Mpc are reported in Table III and show that, while a detection is ideally possible with the current interferometers [the SNR is $\mathcal{O}(1)$], it is unlikely in practice, given the small event rate at such distances, i.e. ≈ 0.01 yr^{-1}. On the other hand, larger SNRs $\mathcal{O}(10)$ can be obtained with advanced detectors. This also means that a detection of these sources up to a distance of 100 Mpc will be possible and so there will a higher event rate. Interestingly, binaries of the same mass, but described by a nonisentropic EOS have a slightly higher SNR and this is simply due to the increase in the delay for the collapse to the BH.

Both the small range in which the masses of NSs fall and the low sensitivity of present detectors in the high-frequency region, where a lot of the power is emitted, underline the importance of the inspiral phase for the detection. This is particularly evident when comparing the large SNR of signals in which the inspiral is a significantly long part. The signal for the high-mass polytropic binary 1.62-60-P starts from an initial separation of 60 km and spans over more than 5 orbits, resulting in a SNR which is a factor of 3 larger than the one of the other binaries, which have an initial separation of 45 km and merge in little more than 2 orbits. This result strongly motivates the investigation, both through simulations and PN approximations, of binaries inspiralling over time scales longer than the already long ones presented here. Stated differently, the study of longer simulations can be used to assess when the lower-order PN expressions are very accurate, while the study of the final part of the inspiral (say the last two orbits) can be used to determine those higher-order PN effects that have not been worked out analytically yet.

V. CONCLUSIONS

We have discussed accurate general-relativistic simulations of binary systems of equal-mass NSs which inspiral starting from irrotational configurations in quasicircular orbit. Spanning over $\sim$30 ms, our simulations are the longest of their kind and provide the first complete (within an idealized treatment of the matter) description of the inspiral and merger of a NS binary leading to the prompt or delayed formation of a BH and to its ringdown.

More specifically, we have considered binary NSs with two different initial masses: low-mass binaries with $M_{\rm ADM} = 2.681 M_\odot$ and high-mass binaries with $M_{\rm ADM} = 2.982 M_\odot$. Such binaries have then been evolved using two different EOSs: namely, an isentropic (i.e. polytropic) EOS and a nonisentropic (i.e. ideal-fluid) EOS. Despite the use of only simple, analytical EOSs, we were able to reproduce some of the aspects that a more realistic EOS would yield. In particular, we have shown that the polytropic EOS leads either to the prompt formation of a rapidly rotating BH surrounded by a dense torus in the high-mass case, or, in the low-mass case, to a HMNS which develops a bar, emits large amounts of gravitational radiation, and eventually experiences a *delayed* collapse to the BH. Conversely, we have shown that the ideal-fluid EOS inevitably leads to a further delay in the collapse to the BH as a result of the larger pressure support provided by the temperature increase via shocks. In this case the temperature in the formed HMNS can reach values as high as 10^{11}–10^{12} K, so that the subsequent dynamics and especially the time of

the collapse can be reduced if cooling mechanisms, such as the direct-URCA process, take place.

With the exception of the low-mass ideal-fluid binary, whose HMNS is expected to collapse to the BH on a time scale which is computationally prohibitive (i.e. $\sim$110 ms), all the binaries considered lead to the formation of a BH surrounded by a rapidly rotating torus. The masses and dimensions of the tori depend on the EOS, but are generically larger than those reported in previous independent studies, with masses up to $\approx 0.07 M_\odot$. Confirming what was reported in Ref. [44], we have found that the amount of angular momentum lost during the inspiral phase can influence the mass of the torus for binaries that have the same EOS. In particular, the models that lose less angular momentum during the inspiral, the comparatively *low-mass* binaries, are expected to have comparatively *high-mass* tori. A more detailed study of the dynamics of the torus (especially when produced from non-equal-mass binaries) and of its implication for short hard GRBs will be the subject of a following paper [90].

Most of the binaries considered have an initial coordinate separation of 45 km and merge after $\sim$2 orbits or, equivalently, after $\sim$6 ms. However, we have also considered a high-mass polytropic binary with an initial coordinate separation of 60 km, which merges after $\sim$5 orbits or, equivalently, after $\sim$20 ms. As a stringent test of the accuracy of our results we have carried out a systematic comparison between identical binaries starting at different initial separations. Such a comparison, which has never been performed before, has shown that there is an excellent agreement in the inspiral phase (as expected from the lowest-order PN approximations), but also small differences at the merger and in the subsequent evolution. These results provide us with confidence on our ability to perform long-term accurate simulations of the inspiral phase, and also open the prospect of investigating higher-order PN corrections.

Besides the study of the bulk dynamics of the two NSs, we have also investigated the small-scale hydrodynamics of the merger and the possibility that dynamical instabilities develop. In this way we have provided the first quantitative description of the onset and development of the Kelvin-Helmholtz instability, which takes place during the first stages of the merger phase, when the outer layers of the stars come into contact and a shear interface forms. The instability curls the interface forming a series of vortices which we were able to resolve accurately using the higher resolutions provided by the AMR techniques. Since the development of this instability is essentially independent of the EOS used or of the masses of the NSs, it could have important consequences in the generation of large magnetic fields. Also this aspect will be further investigated in a subsequent work [90].

Given the importance of binary NSs as sources of gravitational waves, special attention in this work has been dedicated to the analysis of the waveforms produced and to their properties for the different configurations. In particular, we have found that the largest loss rates of energy and angular momentum via gravitational radiation develop at the time of the collapse to the BH and during the first stages of the subsequent ringdown. Nevertheless, the configurations which emit the highest amount of energy and angular momentum are those with lower masses, since they do not collapse promptly to a BH. Instead they produce a violently oscillating HMNS, which emits copious gravitational radiation, while rearranging its angular-momentum distribution, until the advent of the collapse to the BH. We have also found that although the gravitational-wave emission from NS binaries has spectral distributions with large powers at high frequencies (i.e. $f \gtrsim 1$ kHz), a signal-to-noise ratio as large as 3 can be estimated for a source at 10 Mpc using the sensitivity of currently operating gravitational-wave interferometric detectors.

Several aspects of the simulations reported here could be improved and probably the most urgent among them are the use of more realistic EOSs and the inclusion of magnetic fields via the solution of the MHD equations. Recent calculations [48,49] have indeed shown that the corrections produced by strong magnetic fields could be large and are probably very likely to be present. Work is in progress towards these improvements using the code developed in Ref. [51]. The results of these investigations will be presented in forthcoming works.

ACKNOWLEDGMENTS

It is a pleasure to thank the group in Meudon (Paris) for producing and making available the initial data used in these calculations. We are also grateful to N. Dorband, A. Nagar, D. Pollney, and C. Reisswig for help in the calculation of the gravitational waves and to E. Schnetter and all the ''Carpet developers'' for their help with AMR. We thank also R. De Pietri, Y. Eriguchi, G. M. Manca, M. Shibata, and S. Yoshida for useful discussions and comments. The computations were performed on the clusters Peyote, Belladonna, and Damiana of the AEI. This work was supported in part by the DFG Grant No SFB/Transregio 7 and by the JSPS Grant-in-Aid for Scientific Research (No. 19-07803).

APPENDIX A: CHARACTERIZING THE TRUNCATION ERROR

1. The influence of numerical methods

The inherent numerical viscosity of the numerical method used for the reconstruction of the variables on cell interfaces is crucial to determine the time of the merger. As one might expect, lower-order reconstruction schemes result in an anticipated merger due to their higher numerical viscosity, as Fig. 28 shows (for a review of the numerical methods implemented in `Whisky`, see II C).

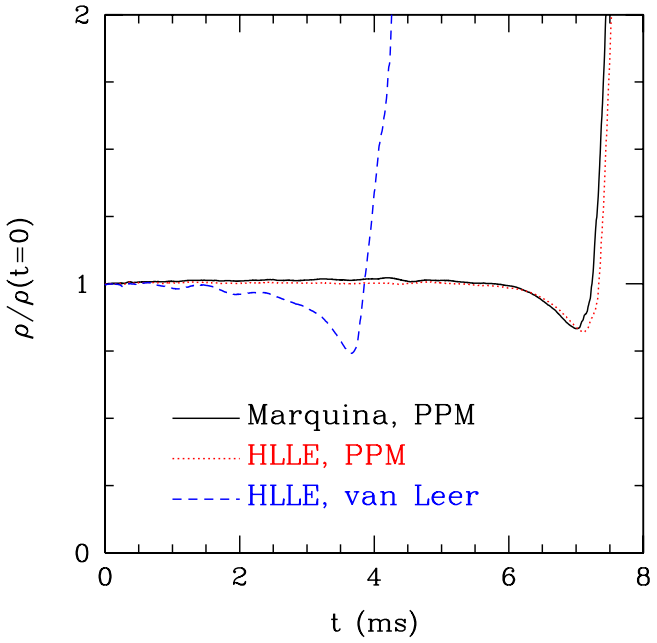

FIG. 28 (color online). Comparison of the rest-mass density normalized to its value at $t = 0$ for evolutions performed with different numerical methods; the solid line refers to an evolution performed using the Marquina flux formula and a PPM reconstruction, the dotted line to HLLE-PPM, and the dashed line to HLLE-TVD (van Leer slope limiter). These data refer to an initial configuration not present in Table I (see text for details) and to an evolution with the ideal-fluid EOS.

The results in the test simulations presented in the figure were produced through the evolution of initial data that are not listed in Table I, i.e. proper separation between the centers of the stars $d/M_{\rm ADM} = 12.6$; baryon mass of each star $M_b = 1.78M_\odot$; total ADM mass $M_{\rm ADM} = 3.24M_\odot$; angular momentum $J = 9.93M_\odot^2 = 8.75 \times 10^{49}$ gcm^2/s; initial orbital angular velocity $\Omega_0 = 9.39 \times 10^{-3} = 1.9$ rad/ms; approximate mean radius of each star $R = 8.4M_\odot = 12$ km; ratio of the polar to the equatorial coordinate radius of each star $r_p/r_e = 0.945$.

In particular, in Fig. 28 we show the differences in the evolution of the rest-mass density normalized to its initial value when different numerical methods are used for the evolution: the solid line refers to an evolution performed using the Marquina flux formula and a PPM reconstruction (which is our usual choice), the dotted line to the HLLE approximate Riemann solver with PPM reconstruction and the dashed line to the HLLE solver with TVD reconstruction (in particular, the van Leer slope limiter was used). Smaller changes in the merger time and in the evolution of the HMNS are observed also by changing some parameters of the PPM reconstruction method, in particular those related to the shock detection, that is the parameters that define how big a jump in the evolved variable has to be, in order to be considered a discontinuity and treated as such.

We have found instead that the choice of approximate Riemann solver does not influence significantly the evolution of the coalescence. As one can see from Fig. 28, when coupled with the PPM reconstruction, both the Marquina and the HLLE solvers produce very similar dynamics and the time of the merger is almost the same. The situation changes when a lower-order reconstruction method, such as the van Leer one, is used. In this case the numerical viscosity is large and the time of the merger is very different, i.e. ≈ 4 ms instead of ≈ 6.5 ms.

From these tests one can then learn that the numerical viscosity of the evolution method is very important in this scenario, being responsible for changes in the dynamics and also in the estimate of the gravitational-wave emission. Of course, one should always employ the least viscous method available.

2. The influence of the initial gauge conditions

We have found that using the shift profile given in the Meudon data introduces a considerable amount of gauge dynamics, which can be avoided by setting the initial shift to zero. We recall that the Meudon shift condition is determined through the Killing equation which is implicit in the quasiequilibrium assumption for binary systems [20]. A clear way to highlight this feature is a comparison of the time evolution of the coordinate separation between the stellar centers. This is shown in Fig. 29, which offers a comparison of the time evolution of the coordinate separation (upper panel) and the proper separation (lower

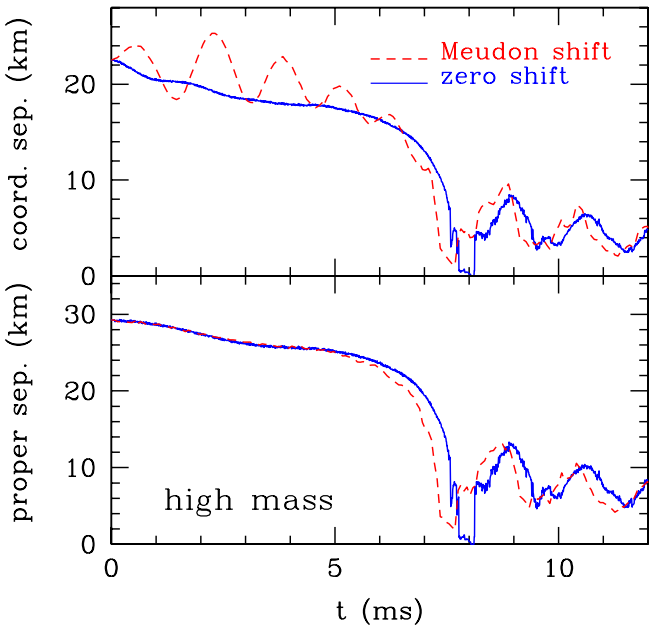

FIG. 29 (color online). Comparison of the time evolution of the coordinate separation (upper panel) and the proper separation (lower panel) between the stellar centers in case the initial Meudon shift is used (dashed line) and in case the initial shift is set to zero (continuous line).

panel) between the stellar centers in case the initial Meudon shift is used (dashed line) and in case the initial shift is set to zero (continuous line). The evolution equation for the shift is the same for the two simulations.

It is clear that the coordinate orbit of the evolution started with the Meudon shift has a noticeable amount of eccentricity (which appears as large oscillations of the coordinate separation of the stars during the inspiral), which is absent in the simulation in which the shift is zero at the initial time. In addition, the adoption of a zero initial shift results into a larger initial violation of the 2-norm of the Hamiltonian constraint, which is, however, below 10^{-6} for the typical resolution used.

As a final remark we note that the proper separations of the stars, the maximum of the rest-mass density, and other gauge-invariant quantities, such as the gravitational waveforms, are instead very similar during the inspiral phase.

[1] J. M. Weisberg, R. W. Romani, and J. H. Taylor, Astrophys. J. **347**, 1030 (1989).
[2] I. Stairs, Z. Arzoumanian, F. Camilo, A. Lyne, D. Nice, J. Taylor, S. Thorsett, and A. Wolszczan, Astrophys. J. **505**, 352 (1998).
[3] M. Kramer, A. Lyne, M. Burgay, A. Possenti, R. Manchester, F. Camilo, M. McLaughlin, D. Lorimer, N. D'Amico, B. Joshi *et al.*, in *Binary Pulsars*, edited by Rasio and Stairs (PSAP, Chicago, 2004).
[4] R. Oechslin, H. T. Janka, and A. Marek, Astron. Astrophys. **467**, 395 (2007).
[5] R. Oechslin and H. T. Janka, Phys. Rev. Lett. **99**, 121102 (2007).
[6] V. Kalogera, C. Kim, D. R. Lorimer, M. Burgay, N. D'Amico, A. Possenti, R. N. Manchester, A. G. Lyne, B. C. Joshi, M. A. McLaughlin *et al.*, Astrophys. J. Lett. **601**, L179 (2004).
[7] F. A. Rasio and S. L. Shapiro, Astrophys. J. **401**, 226 (1992).
[8] M. Ruffert, H.-Th. Janka, and G. Schäfer, Astron. Astrophys. **311**, 532 (1996).
[9] R. Oechslin, S. Rosswog, and F. K. Thielemann, Phys. Rev. D **65**, 103005 (2002).
[10] M. Shibata and K. Uryū, Phys. Rev. D **64**, 104017 (2001).
[11] T. Piran, Phys. Rep. **314**, 575 (1999).
[12] L. Baiotti, R. De Pietri, G. M. Manca, and L. Rezzolla, Phys. Rev. D **75**, 044023 (2007).
[13] G. M. Manca, L. Baiotti, R. D. Pietri, and L. Rezzolla, Classical Quantum Gravity **24**, S171 (2007).
[14] J. C. Lombardi, F. A. Rasio, and S. L. Shapiro, Phys. Rev. D **56**, 3416 (1997).
[15] T. W. Baumgarte, G. B. Cook, M. A. Scheel, S. L. Shapiro, and S. A. Teukolsky, Phys. Rev. D **57**, 7299 (1998).
[16] K. Uryū and Y. Eriguchi, Mon. Not. R. Astron. Soc. **296**, L1 (1998).
[17] S. Bonazzola, E. Gourgoulhon, and J.-A. Marck, Phys. Rev. D **56**, 7740 (1997).
[18] S. Bonazzola, E. Gourgoulhon, and J.-A. Marck, Phys. Rev. Lett. **82**, 892 (1999).
[19] S. Bonazzola, E. Gourgoulhon, and J.-A. Marck, arXiv:gr-qc/9904040.
[20] E. Gourgoulhon, P. Grandclément, K. Taniguchi, J. A. Marck, and S. Bonazzola, Phys. Rev. D **63**, 064029 (2001).
[21] K. Uryū and Y. Eriguchi, Phys. Rev. D **61**, 124023 (2000).
[22] P. Marronetti, G. J. Mathews, and J. R. Wilson, Phys. Rev. D **60**, 087301 (1999).
[23] K. Taniguchi, E. Gourgoulhon, and S. Bonazzola, Phys. Rev. D **64**, 064012 (2001).
[24] K. Taniguchi and E. Gourgoulhon, Phys. Rev. D **65**, 044027 (2002).
[25] K. Taniguchi and E. Gourgoulhon, Phys. Rev. D **66**, 104019 (2002).
[26] K. Taniguchi and E. Gourgoulhon, Phys. Rev. D **68**, 124025 (2003).
[27] T. Nakamura and K. Oohara, arXiv:gr-qc/9812054.
[28] K. C. B. New and J. E. Tohline, Astrophys. J. **490**, 311 (1997).
[29] X. Zhuge, J. M. Centrella, and S. L. W. McMillan, Phys. Rev. D **50**, 6247 (1994).
[30] X. Zhuge, J. M. Centrella, and S. L. W. McMillan, Phys. Rev. D **54**, 7261 (1996).
[31] M. Ruffert, M. Rampp, and H.-Th. Janka, Astron. Astrophys. **321**, 991 (1997).
[32] M. Ruffert, H.-Th. Janka, K. Takahashi, and G. Schaefer, Astron. Astrophys. **319**, 122 (1997).
[33] M. Ruffert and H.-T. Janka, Astron. Astrophys. **380**, 544 (2001).
[34] J. R. Wilson and G. J. Mathews, Phys. Rev. Lett. **75**, 4161 (1995).
[35] G. J. Mathews, P. Marronetti, and J. R. Wilson, Phys. Rev. D **58**, 043003 (1998).
[36] R. Oechslin and H. T. Janka, Mon. Not. R. Astron. Soc. **368**, 1489 (2006).
[37] K.-I. Oohara and T. Nakamura, Prog. Theor. Phys. Suppl. **128**, 183 (1997).
[38] T. Baumgarte, S. Hughes, L. Rezzolla, S. L. Shapiro, and M. Shibata, in *General Relativity and Relativistic Astrophysics Eighth Canadian Conference*, edited by C. Burgess and R. Myers, AIP Conference Proceedings No. 493 (AIP, New York, 1999).
[39] J. A. Font, Living Rev. Relativity **3**, 2 (2000), http://www.livingreviews.org/lrr-2000-2.
[40] J. A. Font, T. Goodale, S. Iyer, M. Miller, L. Rezzolla, E. Seidel, N. Stergioulas, W. M. Suen, and M. Tobias, Phys. Rev. D **65**, 084024 (2002).
[41] M. Shibata, Prog. Theor. Phys. **101**, 1199 (1999).
[42] M. Shibata and K. Uryū, Phys. Rev. D **61**, 064001 (2000).
[43] M. Shibata and K. Uryū, Prog. Theor. Phys. **107**, 265 (2002).

[44] M. Shibata and K. Taniguchi, Phys. Rev. D **73**, 064027 (2006).

[45] M. Anderson, E. W. Hirschmann, L. Lehner, S. L. Liebling, P. M. Motl, D. Neilsen, C. Palenzuela, and J. E. Tohline, Phys. Rev. D **77**, 024006 (2008).

[46] T. Yamamoto, M. Shibata, and K. Taniguchi, Phys. Rev. D **78**, 064054 (2008).

[47] F. A. Rasio and S. L. Shapiro, Classical Quantum Gravity **16**, R1 (1999).

[48] R. H. Price and S. Rosswog, Science **312**, 719 (2006).

[49] M. Anderson, E. W. Hirschmann, L. Lehner, S. L. Liebling, P. M. Motl, D. Neilsen, C. Palenzuela, and J. E. Tohline, Phys. Rev. Lett. **100**, 191101 (2008).

[50] Y. T. Liu, S. L. Shapiro, Z. B. Etienne, and K. Taniguchi, Phys. Rev. D **78**, 024012 (2008).

[51] B. Giacomazzo and L. Rezzolla, Classical Quantum Gravity **24**, S235 (2007).

[52] L. Baiotti, I. Hawke, P. Montero, and L. Rezzolla, in *Computational Astrophysics in Italy: Methods and Tools*, edited by R. Capuzzo-Dolcetta (Mem. Soc. Astron. It. Suppl., Trieste, 2003), Vol. 1, p. 210.

[53] L. Baiotti, I. Hawke, P. J. Montero, F. Löffler, L. Rezzolla, N. Stergioulas, J. A. Font, and E. Seidel, Phys. Rev. D **71**, 024035 (2005).

[54] T. Nakamura, K. Oohara, and Y. Kojima, Prog. Theor. Phys. Suppl. **90**, 1 (1987).

[55] M. Shibata and T. Nakamura, Phys. Rev. D **52**, 5428 (1995).

[56] T. W. Baumgarte and S. L. Shapiro, Phys. Rev. D **59**, 024007 (1998).

[57] M. Alcubierre, B. Brügmann, T. Dramlitsch, J. A. Font, P. Papadopoulos, E. Seidel, N. Stergioulas, and R. Takahashi, Phys. Rev. D **62**, 044034 (2000).

[58] J. W. York, in *Sources of Gravitational Radiation*, edited by L. L. Smarr (Cambridge University Press, Cambridge, England, 1979), p. 83, ISBN 0-521-22778-X.

[59] M. Alcubierre, B. Brügmann, P. Diener, M. Koppitz, D. Pollney, E. Seidel, and R. Takahashi, Phys. Rev. D **67**, 084023 (2003).

[60] M. Shibata, Phys. Rev. D **60**, 104052 (1999).

[61] C. W. Misner, K. S. Thorne, and J. A. Wheeler, *Gravitation* (Freeman, San Francisco, 1973).

[62] C. Bona, J. Massó, E. Seidel, and J. Stela, Phys. Rev. Lett. **75**, 600 (1995).

[63] J. G. Baker, J. Centrella, D.-I. Choi, M. Koppitz, and J. van Meter, Phys. Rev. Lett. **96**, 111102 (2006).

[64] J. van Meter, J. G. Baker, M. Koppitz, and D.-I. Choi, Phys. Rev. D **73**, 124011 (2006).

[65] M. Koppitz, D. Pollney, C. Reisswig, L. Rezzolla, J. Thornburg, P. Diener, and E. Schnetter, Phys. Rev. Lett. **99**, 041102 (2007).

[66] T. Goodale, G. Allen, G. Lanfermann, J. Massó, T. Radke, E. Seidel, and J. Shalf, in *Vector and Parallel Processing—VECPAR'2002, 5th International Conference, Lecture Notes in Computer Science* (Springer, Berlin, 2003).

[67] D. Pollney, C. Reisswig, L. Rezzolla, B. Szilágyi, M. Ansorg, B. Deris, P. Diener, E. N. Dorband, M. Koppitz, A. Nagar, *et al.*, Phys. Rev. D **76**, 124002 (2007).

[68] J. M. Martí, J. M. Ibáñez, and J. A. Miralles, Phys. Rev. D **43**, 3794 (1991).

[69] F. Banyuls, J. A. Font, J. M. Ibáñez, J. M. Martí, and J. A. Miralles, Astrophys. J. **476**, 221 (1997).

[70] J. Ibáñez, M. Aloy, J. Font, J. Martí, J. Miralles, and J. Pons, in *Godunov Methods: Theory and Applications*, edited by E. Toro (Kluwer Academic/Plenum Publishers, New York, 2001).

[71] J. A. Font, Living Rev. Relativity **6**, 4 (2003).

[72] E. F. Toro, *Riemann Solvers and Numerical Methods for Fluid Dynamics* (Springer-Verlag, Berlin, 1999).

[73] S. A. Teukolsky, Phys. Rev. D **61**, 087501 (2000).

[74] G. Leiler and L. Rezzolla, Phys. Rev. D **73**, 044001 (2006).

[75] A. Harten, B. Engquist, S. Osher, and S. R. Chakrabarty, J. Comput. Phys. **71**, 231 (1987).

[76] P. Colella and P. R. Woodward, J. Comput. Phys. **54**, 174 (1984).

[77] A. Harten, P. D. Lax, and B. van Leer, SIAM Rev. **25**, 35 (1983).

[78] P. L. Roe, J. Comput. Phys. **43**, 357 (1981).

[79] M. A. Aloy, J. M. Ibáñez, J. M. Martí, and E. Müller, Astrophys. J. Suppl. Ser. **122**, 151 (1999).

[80] E. Schnetter, S. H. Hawley, and I. Hawke, Classical Quantum Gravity **21**, 1465 (2004).

[81] S. Fromang and J. Papaloizou, Astron. Astrophys. **476**, 1113 (2007).

[82] J. Thornburg, Classical Quantum Gravity **21**, 743 (2004).

[83] L. Baiotti and L. Rezzolla, Phys. Rev. Lett. **97**, 141101 (2006).

[84] L. Baiotti, I. Hawke, and L. Rezzolla, Classical Quantum Gravity **24**, S187 (2007).

[85] L. Baiotti, I. Hawke, L. Rezzolla, and E. Schnetter, Phys. Rev. Lett. **94**, 131101 (2005).

[86] H. O. Kreiss and J. Oliger, *Methods for the Approximate Solution of Time Dependent Problems* GARP Publications Series No. 10 (WMO-ICSU, Geneva, 1973).

[87] L. Bildsten and C. Cutler, Astrophys. J. **400**, 175 (1992).

[88] http://www.lorene.obspm.fr.

[89] H. Shen, H. Toki, K. Oyamatsu, and K. Sumiyoshi, Nucl. Phys. **A637**, 435 (1998).

[90] L. Baiotti, B. Giacomazzo, and L. Rezzolla (unpublished).

[91] E. Evans, A. Gopakumar, P. Gressman, S. Iyer, M. Miller, W.-M. Suen, and H.-M. Zhang, Phys. Rev. D **67**, 104001 (2003).

[92] G. J. Mathews and J. R. Wilson, Phys. Rev. D **61**, 127304 (2000).

[93] T. W. Baumgarte, G. B. Cook, M. A. Scheel, S. L. Shapiro, and S. A. Teukolsky, Phys. Rev. Lett. **79**, 1182 (1997).

[94] T. W. Baumgarte, G. B. Cook, M. A. Scheel, S. L. Shapiro, and S. A. Teukolsky, Phys. Rev. D **57**, 6181 (1998).

[95] P. J. Montero, O. Zanotti, J. A. Font, and L. Rezzolla, Mon. Not. R. Astron. Soc. **378**, 1101 (2007).

[96] O. Zanotti, J. A. Font, L. Rezzolla, and P. J. Montero, Mon. Not. R. Astron. Soc. **356**, 1371 (2005).

[97] E. Rubio-Herrera and W. H. Lee, Mon. Not. R. Astron. Soc. **357**, L31 (2005).

[98] E. Rubio-Herrera and W. H. Lee, Mon. Not. R. Astron. Soc. **362**, 789 (2005).

[99] P. J. Montero, O. Zanotti, J. A. Font, and L. Rezzolla, Mon. Not. R. Astron. Soc. **378**, 1101 (2007).

[100] L. Rezzolla, S. Yoshida, T. J. Maccarone, and O. Zanotti, Mon. Not. R. Astron. Soc. **344**, L37 (2003).

[101] L. Rezzolla, S. Yoshida, and O. Zanotti, Mon. Not. R. Astron. Soc. **344**, 978 (2003).
[102] A. Ashtekar and B. Krishnan, Living Rev. Relativity **7**, 10 (2004), http://www.livingreviews.org/lrr-2004-10.
[103] O. Dreyer, B. Krishnan, D. Shoemaker, and E. Schnetter, Phys. Rev. D **67**, 024018 (2003).
[104] M. Campanelli, C. O. Lousto, and Y. Zlochower, Phys. Rev. D **73**, 061501(R) (2006).
[105] L. Rezzolla, E. N. Dorband, C. Reisswig, P. Diener, D. Pollney, E. Schnetter, and B. Szilágyi, Astrophys. J. **708**, 1422 (2007).
[106] L. Rezzolla, P. Diener, E. N. Dorband, D. Pollney, C. Reisswig, E. Schnetter, and J. Seiler, Astrophys. J. **674**, L29 (2008).
[107] L. Rezzolla, E. Barausse, E. N. Dorband, D. Pollney, C. Reisswig, J. Seiler, and S. Husa, Phys. Rev. D **78**, 044002 (2008).
[108] L. Blanchet, Living Rev. Relativity **5**, 3 (2002), http://www.livingreviews.org/lrr-2002-3.
[109] N. Stergioulas, T. A. Apostolatos, and J. A. Font, Mon. Not. R. Astron. Soc. **352**, 1089 (2004).
[110] H. Dimmelmeier, N. Stergioulas, and J. A. Font, Mon. Not. R. Astron. Soc. **368**, 1609 (2006).
[111] M. Shibata and K. Taniguchi, Phys. Rev. D **77**, 084015 (2008).
[112] M. Shibata, Y. Sekiguchi, and R. Takahashi, Prog. Theor. Phys. **118**, 257 (2007).
[113] B. D. Farris, T. K. Li, Y. T. Liu, and S. L. Shapiro, Phys. Rev. D **78**, 024023 (2008).
[114] S. L. Shapiro and S. A. Teukolsky, *Black Holes, White Dwarfs, and Neutron Stars* (John Wiley & Sons, New York, 1983).
[115] J. M. Lattimer, C. J. Pethick, M. Prakash, and P. Haensel, Phys. Rev. Lett. **66**, 2701 (1991).
[116] M. Saijo and Y. Kojima, Phys. Rev. D **77**, 063002 (2008).
[117] S. Chandrasekhar, *Hydrodynamic and Hydromagnetic Stability* (Dover, New York, 1981).
[118] S. Teukolsky, Astrophys. J. **504**, 442 (1998).
[119] L. Gunnarsen, H. Shinkai, and K. Maeda, Classical Quantum Gravity **12**, 133 (1995).
[120] S. A. Teukolsky, Astrophys. J. **185**, 635 (1973).
[121] A. M. Abrahams, L. Rezzolla, M. E. Rupright, A. Anderson, P. Anninos, T. W. Baumgarte, N. T. Bishop, S. R. Brandt, J. C. Browne, K. Camarda, *et al.*, Phys. Rev. Lett. **80**, 1812 (1998).
[122] M. E. Rupright, A. M. Abrahams, and L. Rezzolla, Phys. Rev. D **58**, 044005 (1998).
[123] L. Rezzolla, A. M. Abrahams, R. A. Matzner, M. E. Rupright, and S. L. Shapiro, Phys. Rev. D **59**, 064001 (1999).
[124] V. Moncrief, Ann. Phys. (N.Y.) **88**, 323 (1974).
[125] A. M. Abrahams and R. H. Price, Phys. Rev. D **53**, 1963 (1996).
[126] A. Nagar and L. Rezzolla, Classical Quantum Gravity **22**, R167 (2005); **23**, 4297(E) (2006).
[127] P. Ajith, S. Babak, Y. Chen, M. Hewitson, B. Krishnan, J. T. Whelan, B. Brügman, J. Gonzalez, M. Hannam, S. Husa, *et al.*, Classical Quantum Gravity **24**, S689 (2007).
[128] P. Ajith, S. Babak, Y. Chen, M. Hewitson, B. Krishnan, A. M. Sintes, J. T. Whelan, B. Brugman, P. Diener, N. Dorband, *et al.*, Phys. Rev. D **77**, 104017 (2008).
[129] A. Nagar, O. Zanotti, J. A. Font, and L. Rezzolla, Phys. Rev. D **75**, 044016 (2007).
[130] E. Leaver, Proc. R. Soc. A **402**, 285 (1985).
[131] F. Echeverria, Phys. Rev. D **40**, 3194 (1989).